Androgen receptor imprints satellite cells stemness and preserves their reservoir for lifelong regeneration and optimal repair

Joe G. Rizk[1*], Kamar C. Ghaibour[1*], Sirine Souali-Crespo[1], Aurore Bilger[1], Emilia Calvano[1], Hugues Jacobs[1], Nadia Messaddeq[1], Qingshuang Cai[1], Erwan Grandgirard[1], Rajesh Sahu[1], Arnaud Ferry[2], Gianni Zanardelli[1], Nacho Molina[1], Coralie Fontaine[3], Jean-François Arnal[3], Daniel Metzger[1], Delphine Duteil[1#]

[1] Université de Strasbourg, CNRS, Inserm, IGBMC UMR 7104- UMR-S 1258, F-67400 Illkirch, France

[2] Centre de Recherche en Myologie, UMRS974-Sorbonne Université-INSERM U974-Association Institut de Myologie, France.

[3] Institut National de la Santé et de la Recherche Médicale (INSERM), U1297, Institut des Maladies Métaboliques et Cardiovasculaires (I2MC), Université Toulouse III Paul Sabatier, CHU Rangueil (University Hospital) de Toulouse, F-31432 Toulouse, France

[#] Author to whom correspondence should be addressed at duteild@igbmc.fr.

[*] These authors equally contributed to this work.

SUMMARY

Skeletal muscle stem cells (MuSC) are the guardians of muscle regeneration, sustaining tissue integrity through a delicate balance of quiescence, activation, and lineage commitment. While numerous molecular cues have been implicated in regulating these processes, the influence of androgen receptor (AR) signaling, an essential hormonal pathway for male muscle physiology, has remained largely unexplored. Here, we show that AR expression defines quiescent MuSC and acts as a safeguard of their dormancy. Integrated multi-omic analyses reveal a redistribution of AR binding from quiescence-maintenance loci to regulatory elements driving activation and metabolic reprogramming during repair. Loss of AR at puberty disrupts this balance, precipitating premature cell-cycle entry, skewed divisions toward symmetric differentiation, depletion of the stem cell reservoir, and destabilization of the niche. These defects converge with hallmarks of aging-associated androgen decline, while androgen supplementation restores regenerative competence. Together, our findings establish AR signaling as a pivotal determinant of MuSC fate and a cornerstone of skeletal muscle homeostasis.

KEY WORDS

Satellite Cells, Androgen Receptor, Androgens, Skeletal Muscle, Regeneration, Ageing, Symmetric differentiation

INTRODUCTION

Skeletal muscles exhibit a remarkable regeneration capacity upon injury, resulting from the fusion of newly formed myocytes to generate myofibers that replace the damaged ones. This process is initiated by myofiber degeneration, causing inflammatory cell infiltration followed by the activation of satellite cells, which are the muscle stem cells (MuSC) [1]. In the intact muscle, MuSC reside in a quiescent state within a specialized niche between the myofiber sarcolemma and the basal lamina [2, 3]. They are defined by the expression of the myogenic transcription factor paired box 7 (*Pax7*), a key marker of their identity and function [4].

Upon muscle injury, MuSC exhibit a dual capacity. They can either self-renew to replenish the stem cell pool and preserve long-term regenerative competence, or enter a proliferative phase followed by activation of the myogenic differentiation program, culminating in fusion and formation of new myofibers [5, 6]. These key myogenic features, are intrinsically dependent on MuSC microenvironment, comprising immune and stromal cells. This microenvironment is tightly regulated by interactions with extracellular matrix components, inter-cell signaling and paracrine or endocrine stimuli [7-9]. With age, skeletal muscle regenerative capacities progressively decline, which has been recently attributed to a reduction in MuSC number and function [10, 11]. These processes are thought to be exacerbated by hormonal changes, including decrease in circulating androgens [12-14].

Androgens are steroid hormones mainly produced by male gonads. They play a crucial role in modulating muscle homeostasis and MuSC fate, both during postnatal development and at adult stages [15, 16]. At puberty, androgens promote MuSC quiescence through a Notch-dependent pathway [17], and influence their activation, proliferation, and differentiation [17-19]. In addition, androgen supplementation increases MuSC numbers in both animal models and humans [20]. Oppositely, castration-induced androgen deprivation in rodents leads to perturbed MuSC homeostasis [21]. Androgens exert their effects through the androgen receptor (AR), a ligand-activated transcription factor and member of the nuclear receptor superfamily, which upon ligand binding translocates to the nucleus and binds specific DNA sequences known as androgen response elements (AREs), to regulate target genes expression [22-24]. We previously showed that AR in myofibers is instrumental for the musculoskeletal system by controlling gene networks required for structural and metabolic demands [24, 25]. Nevertheless, the role of androgens *via* AR in MuSC during muscle regeneration at puberty, the broader consequences of androgen decline on the regenerative machinery, the underlying molecular mechanisms, and its potential causal link to age-associated muscle degeneration remain to be fully delineated.

By integrating genome-wide profiling and histological analysis, with the study of an inducible MuSC-specific AR knockout mouse model and stem-like myogenic cell lines, we delineate the molecular

mechanisms through which androgens *via* their receptor regulate MuSC regenerative functions. Our findings highlight the pivotal role of MuSC-AR in muscle repair, identifying AR-dependent stem cell profiles and supportive MuSC subtypes involved in postnatal myogenesis. We further reveal that AR orchestrates stemness transitions by sequential chromatin repositioning following injury, thereby controlling gene networks governing MuSC self-renewal, proliferation, and differentiation. Additionally, we demonstrate that androgen signaling contributes to the age-related decline in muscle healing capacities, and validate the translational relevance of murine findings in human myoblasts.

RESULTS

AR deficiency in MuSC at puberty compromises regenerative capacity and alters metabolic and structural transcriptional programs in skeletal muscle

To dissect the specific role of AR signaling within MuSC at puberty, we generated mice with a conditional AR deletion in this cell lineage (hereafter $AR^{(i)sat-/Y}$ mice). Nine-week-old mice harboring floxed *Ar* alleles and expressing the *Pax7*-$CreER^{T2}$ transgene were treated with tamoxifen (TAM) for 5 days, enabling selective deletion of *Ar* in MuSC (Figures S1A- S1C). TAM-treated littermates lacking the *Pax7*-$CreER^{T2}$ transgene served as controls. To evaluate the functional consequences of AR ablation on skeletal muscle regenerative capacities, we subjected control and $AR^{(i)sat-/Y}$ mice to acute TA muscle injury *via* cardiotoxin (CTX) injection one month after gene ablation, and assessed histological features of repair at 5-, 7-, 14-, and 28-days post-injury (dpi).

At 5 dpi, both genotypes showed similar hallmarks of effective regeneration, including centronucleated fibers, necrosis, and immune cell infiltration (Figure S1D). However, at 7, 14, and 28 dpi, $AR^{(i)sat-/Y}$ mice exhibited regenerative defects, including persistent inflammation, and aberrant fiber morphology (Figures 1A and S1D). Ultrastructural analyses performed at 7 dpi revealed that $AR^{(i)sat-/Y}$ muscles displayed disorganized sarcomeres, with misaligned triads characterized by dilated T-tubules, disrupted Z-lines, and poorly defined or absent M-lines (Figure 1B). These structural muscle defects correlated with a significant reduction in myofiber cross-sectional area (Figure 1C), which translated into a significant reduction in contractile force at 28 dpi (Figure 1D). Muscle dysfunctions were also accompanied by a significant reduction in the MuSC pool 7 dpi (Figures 1E and 1F), showing that loss of AR in MuSC severely impairs regenerative capacity in young male mice.

To elucidate the transcriptional landscape regulated by AR in MuSC and their progeny during skeletal muscle regeneration at puberty, we conducted bulk RNA sequencing (RNA-seq) on tibialis anterior (TA) muscles harvested at 7 dpi from young $AR^{(i)sat-/Y}$ and control mice. Our analysis revealed a differential expression of 3,586 genes, comprising 2,045 downregulated and 1,541 upregulated genes in AR-deficient mice (Figures 1G and S1E). Pathway analyses of the downregulated genes highlighted a strong association with biological processes involved in actin cytoskeleton organization, focal adhesion, and developmental signaling cascades such as the PI3K-Akt pathway (Figure 1H). Strikingly, the expression of key myogenic regulators, including *Pax7*, *Myf5*, *Myod1*, *Myog*, fusion-mediating factors such as *Myomixer* (*Mymx*) and *Myomaker* (*Mymk*) was markedly reduced in $AR^{(i)sat-/Y}$ muscles (Figure 1I), in agreement with the decreased MuSC number. Similarly, transcripts encoding contractile cytoskeletal components such as actin, actinin, troponin and tropomyosin isoforms (e.g. *Actb*, *Actn1*, *Actn4*, *Tnnc1*, *Tnnt2*, *Tpm3*), and embryonic myosin heavy chains isoforms (*Myh3*, embryonic and *Myh8*, perinatal), as well as non-contractile components, including laminins (*Lmna*), *Myomesin 3*

(*Myom3*), and *Dystrophin* (*Dmd*), were significantly diminished (Figures 1G and 1I), providing a molecular rationale for the morphological abnormalities observed at this timepoint. In agreement, immunofluorescence analysis of DMD at 7 dpi revealed profound structural abnormalities in $AR^{(i)sat-/Y}$ mice compared to control littermates (Figure 1J). Moreover, co-staining for sarcomeric alpha actinin (ACTN1) and DMD on transverse sections showed disrupted sarcomere alignment and uneven ACTN1 distribution in mutant fibers, while longitudinal sections confirmed major striation defaults (Figure 1K, pink arrows). Notably, whereas healing control fibers had centrally positioned nuclei, $AR^{(i)sat-/Y}$ fibers showed disorganized central nuclear localization (Figure 1K, white arrows), reflecting a disrupted cytoskeletal organization. Consistent with our transcriptomic data, immunostaining for embryonic myosin heavy chain (MYH3) at 5 and 7 dpi showed a ~50% reduction in the number of MYH3-positive fibers in $AR^{(i)sat-/Y}$ mice compared to controls (Figures 1L and 1M), signifying delayed or incomplete myogenic progression. To further investigate this impairment, we examined the expression profile of myosin heavy chain isoforms (Figure 1N). In contrast to the downregulation of *Myh3* and *Myh8*, transcripts of *Myh2*, *Myh4*, and *Myh7* (encoding MyHC IIa, IIb, and I, respectively) were upregulated (Figure 1N), reflecting a shift toward increased expression of adult myosin heavy chain isoforms at the expense of fetal ones, although *Myh1* (MyHC IIx) did not reach statistical significance (Figure 1N). Interestingly, transcriptomic analysis of the 1,541 genes upregulated in 7 dpi-injured $AR^{(i)sat-/Y}$ TA muscles revealed a predominant enrichment in metabolic pathways, particularly those governing glycolysis, oxidative phosphorylation, mitochondrial function, and the metabolism of glycogen, fatty acids, and amino acids (Figure 1H). Notably, expression of several key regulators of cellular metabolism, including aconitase 2 (*Aco2*), citrate synthase (*Cs*), and multiple isoforms of isocitrate dehydrogenase (e.g. *Idh2* and *Idh3a*), was markedly elevated in $AR^{(i)sat-/Y}$ muscles. This was paralleled by increased expression of genes and components of the oxidative phosphorylation machinery, including most of the members of mitochondrial complex I (e.g., *Ndufa1-13*), II (e.g., *Sdha-d*), III (e.g., *Uqcrc1-2*), IV (e.g., *Cox5a*, and *Cox10a*), and V (e.g., *Atp5a1* and *Atp5b*) (Figure 1O).

To investigate whether the absence of MuSC-AR during regeneration promotes a metabolic shift toward a more oxidative muscle fiber phenotype, we stained NADH dehydrogenase activity (NADH-DH) 7 dpi. In regenerating TA muscles from control mice, we observed lightly stained fibers, indicative of glycolytic metabolism. In contrast, $AR^{(i)sat-/Y}$ muscles displayed a higher presence of darkly stained fibers (Figure 1P), reflecting increased NADH-DH activity. These findings were corroborated by cytochrome c oxidase (COX) activity staining, indicative of a glycolytic-to-oxidative shift in fiber type composition (Figure 1P). These findings prompted us to investigate whether such metabolic alterations are intrinsically rooted in MuSC. Seahorse analysis performed on LHCN-M2 myoblasts, treated with 100 nM of the AR antagonist flutamide, unveiled an increased oxidative phosphorylation

activity when compared to vehicle-treated cells (Figure 1Q and S1F) indicating that the metabolic abnormalities observed in regenerating myofibers may originate from intrinsic defects in MuSC. Altogether, our data show that AR loss at puberty leads to MuSC depletion and important structural defects, associated with a fiber-type switch towards oxidative metabolism.

Androgen signaling in MuSC coordinates gene programs essential for homeostasis and regeneration

To elucidate the cell-specific AR-dependent molecular mechanisms governing MuSC homeostasis during skeletal muscle regeneration at puberty, we performed a SMART-seq on FACS-isolated MuSC from 7 dpi-injured TA of control and $AR^{(i)sat-/Y}$ male mice. Transcriptomic analysis revealed differential expression of 821 genes in AR-deficient MuSC, including 327 down- and 494 upregulated genes (Figures 2A and S2A). Consistent with the Seahorse assay findings and the histological evidence of a metabolic shift toward oxidative metabolism at 7 dpi, analysis of the upregulated genes highlighted a strong enrichment of pathways related to metabolic processes, particularly cellular respiration and oxidative phosphorylation (Figure 2B). In particular, the expression of *Cox5b* and *Cox6b1*, in addition to numerous genes implicated in mitochondrial homeostasis, was significantly elevated in $AR^{(i)sat-/Y}$ MuSC (Figure 2C). Conversely, pathway analysis of the downregulated gene set revealed a significant association with cell cycle regulation (e.g., DNA replication and cell division) (Figure 2B).

To identify the direct transcriptional targets of AR, we isolated MuSC from TA muscles of 3-month-old control mice by FACS at 7 dpi , and performed CUT&RUN assays using AR-specific antibodies, alongside profiling of demethylated histone H3 (H3K4me2), a well-established marker of active promoters and enhancers. Bioinformatic analysis identified 7,346 AR-binding peaks, predominantly located within intronic and intergenic regions encompassing the canonical androgen response elements (AREs) (Figures 2D and S2B), as well as 39,900 peaks associated with the H3K4me2 mark, evenly distributed between promoter, intron and intergenic regions (Figure S2C). Integrative analysis of the two datasets revealed that AR is directly recruited to 3,104 transcribed genes (Figure S2D). Gene ontology and pathway enrichment analyses of AR-bound genes uncovered a strong association with key developmental and regenerative pathways, including the HIPPO (e.g. *Tead1*, *Wwc1*, *Fat4*) and WNT signaling cascades (e.g. *Wnt5a*, *Fzd4*), as well as signaling modules related to tissue remodeling and regeneration, such as cell adhesion, focal adhesion, extracellular matrix (ECM)-receptor interactions, and actin cytoskeleton regulation (Figure 2E). Notably, AR occupancy was also observed at genes essential for stem cell homeostasis (e.g. *Foxo1*, *Bcl2*), muscle repair (e.g. *Mstn*, *Cxcl2*, *Cdh15*), and sarcomere assembly or function (e.g. *Myh1*, *Mylk4*, *Myom2*). A transcription start site (TSS) gene-centric analysis demonstrated that AR binds more than the two-thirds of both down- and upregulated genes in $AR^{(i)sat-/Y}$ mice within a 100-kb window (Figure 2F), showing that AR predominantly regulates

gene expression through distal elements. Representative AR binding loci within key genes involved in the aforementioned pathways, including *Ar* itself, *Fzd4*, *Kdmc4*, *Myh1, Tead1*, and *Mylk4* are illustrated in Figure 2G. Gene ontology analysis revealed that genes downregulated in association with AR peaks at 7 dpi were predominantly involved in cellular structural and organelle-related processes (Figure S2E), whereas upregulated genes were enriched in metabolic pathways (Figure S2F), thereby providing a molecular basis for the impaired phenotype observed at the histological level. Altogether, these findings support a model in which AR orchestrates regenerative transcriptional programs in MuSC via enhancer-driven mechanisms at puberty.

Single-cell RNA sequencing reveals early molecular and cellular alterations in the AR-deficient MuSC microenvironment

To decipher the primary events underlying defective MuSC homeostasis caused by AR loss, and the consequent impact on their microenvironment during impaired regeneration, we performed single-cell RNA sequencing (scRNA-seq) in 5-dpi-injured TA muscles of 3-month-old control and $AR^{(i)sat-/Y}$ mice (Figure S3A). Of note, $AR^{(i)sat-/Y}$ mice harbored the YFP transgene selectively in MuSC to efficiently follow those cells. We identified 12 unsupervised clusters, annotated to the literature [26, 27], based on the expression of specific marker genes (Figures 3A and S3B), with no evidence of cell population loss or emergence in mutants (Figures 3A and 3B). However, we observed a slight reduction in the proportion of fibro-adipogenic progenitors (FAPs) and MuSC, as well as an increase in that of both macrophages in $AR^{(i)sat-/Y}$ mice compared to controls (Figure 3B). Flow cytometry analysis of injured TA muscles at 5 dpi, furtherly confirmed a ~30% increase in macrophages number (Figure 3C), and ~8% decrease of MuSC, even though total immune cells and FAPs were not significantly altered (Figure 3D). Notably, *Ar* expression was not ubiquitous across all populations; rather, it was predominantly detected in cell types exhibiting stem-like properties or mesenchymal profiles, including FAPs, fibroblasts, and MuSC (Figure 3E). Of note, *Ar* expression was completely abolished in mutant MuSC, and not in other cell types (Figure 3E), while *Yfp* was exclusively expressed in MuSC of $AR^{(i)sat-/Y}$ mice, consistent with the genetic engineering of our model (Figure S3C). Moreover, AR deficiency in MuSC strongly altered the transcriptional profile of their microenvironment (Figure S3D).

To assess intercellular communication within injured muscle tissue at 5 dpi, we employed CellChat analysis on scRNA-seq data. In control mice, this analysis revealed a highly interconnected signaling network encompassing all cellular populations, indicative of active and coordinated crosstalk during the regenerative process (Figures S3E and S3F). Interestingly, communication within the MuSC population was diminished in $AR^{(i)sat-/Y}$ mice (Figure 3F), pointing to a disruption in intra-population signaling.

Given the critical interplay between MuSC, macrophages, and FAPs, we next examined the gene networks affected by MuSC-AR loss within these two cell populations. Functional enrichment analysis of the 1,707 differentially expressed genes upon AR loss in MuSC within macrophages uncovered a transcriptional landscape indicative of macrophages homeostasis (Figure S3G). In particular, transcripts encoding core components of the inflammasome pathway, including caspase 1 (*Casp1*) and its adaptor *Pycard*, were elevated, alongside the chemokines C-C motif chemokine ligand 2 (*Ccl2*) and C-X-C motif chemokine ligand 10 (*Cxcl10*), both of which are known to promote monocyte recruitment. Furthermore, we observed enrichment in metabolic and proteasome pathways intimately linked with immune regulation and tissue remodeling, including oxidative phosphorylation (e.g., *Cox6b1, Cox17*), and ubiquitin-proteasome mediated degradation (e.g., *Uba3*) (Figure S3G). Moreover, macrophage polarization analysis revealed robust expression of canonical M1 (pro-inflammatory) markers including *Il1b* and *Tnf*, in both control and mutant macrophages at 5 dpi (Figure 3G). In contrast, macrophages from $AR^{(i)sat-/Y}$ mice expressed anti-inflammatory (M2-like) markers such as interleukin-10 (*Il10*) and peroxisome proliferator-activated receptor gamma (*Pparg*), suggesting a precocious transition toward an anti-inflammatory phenotype in mutant individuals (Figure 3H). To determine whether this aberrant immune environment persists over time, we extended our analysis to 7 dpi. Flow cytometry revealed a three-fold increase in immune cells in $AR^{(i)sat-/Y}$ TA relative to controls (Figure 3I), which was confirmed by the immunofluorescent labeling of the macrophage-specific marker F4/80 (Figure 3J, white arrows). Remarkably, macrophages were frequently localized inside degenerating muscle fibers of $AR^{(i)sat-/Y}$ mice (Figure 3J, yellow arrows), a phenomenon typically restricted to early regenerative stages, thus indicating delayed resolution of inflammation or prolonged clearance of necrotic tissue. Together, these findings reveal that AR signaling in MuSC plays a pivotal role in modulating the inflammatory response within the injured muscle by impacting the macrophage transcriptomic repertoire.

To unravel the impact of AR loss in MuSC on FAPs transcriptional signature, we performed further functional enrichment analysis of their 976 differentially expressed genes (Figure S3H). Pathway analysis revealed upregulation of fibrosis-related transcripts, including *Tgfb*, alongside extracellular matrix (ECM) remodeling enzymes, such as *Adamts* isoforms, *Mmp19*, *Serpine1*, and *Cthrc1*. Moreover, we observed enhanced expression of key adipogenic regulators (*Zeb1*, *Cebpd*, *Socs1*, and *Socs3*). Functional enrichment also highlighted disruptions in metabolic pathways, notably oxidative phosphorylation (*Cox4i1*, *Cox5a*, *Cox6a1*) and aerobic respiration (*Aco2*, *Hadhb*, *Gls*, *Lipa*) (Figure S3H), pointing toward a shift in FAPs identity, from pro-regenerative to fibrotic and adipogenic. Interestingly, while FAPs numbers were comparable between genotypes at 5 dpi (Figure 3D), a two-fold reduction was observed in $AR^{(i)sat-/Y}$ muscles by 7 dpi (Figure 3I). We therefore postulated that

decline might be attributed to differentiation of FAPs towards the fibrogenic or adipogenic lineages. To this aim, we performed Sirius Red staining at 7 dpi on injured TA from control and mutant mice. Mutant muscles displayed a marked increase in collagen deposition, with fibrotic area nearly doubled compared to controls (Figures 3K and 3L, black arrows). These findings were corroborated by Masson's Trichrome staining, which revealed a significant enrichment of collagen within the ECM at 7 dpi, with signs of early deposition already evident at 5 dpi in young $AR^{(i)sat-/Y}$ mice (Figure S3I). Polarized light microscopy revealed that the qualitative composition of the ECM, including collagenous components such as collagens type I (Figure 3M, white arrows) and III (Figure 3L, blue arrows), and non-collagenous cones (e.g., fibronectin, laminins, elastin, tenascin-C, and proteoglycans) remained comparable between genotypes (Figures 3K and 3L), indicating a quantitative rather than compositional remodeling. We further evaluated adipogenic conversion via perilipin-1 (PLIN1) immunostaining. At 5 dpi, $AR^{(i)sat-/Y}$ muscles already exhibited discrete adipocyte emergence (Figure 3N, white arrows), which became markedly more pronounced by 7 dpi, while control muscles remained largely devoid of PLIN1-positive cells (Figure 3N).

Thus, our data demonstrate that AR loss in MuSC impacts FAPs differentiation capacities promoting fibrosis and adipogenesis. Altogether, loss of AR signaling in MuSC at puberty disrupts key interactions within the regenerative microenvironment, altering intercellular communication, immune dynamics, and FAP fate (Figure 3O).

AR deficiency in MuSC at puberty perturbs their stemness signatures, disrupts their commitment, and impairs their differentiation potential

Strikingly, only few genes were differentially expressed in MuSC, suggesting that different cell populations might lay in this cluster. To further explore the transcriptional changes between control and $AR^{(i)sat-/Y}$ MuSC, we subclustered a total of 2,078 MuSC (Figures S4A and S4B). Unsupervised clustering revealed six distinct MuSC subpopulations (Figure S4B), of which two clusters exhibited an immune signature characterized by the expression of *C1qc*, *Lyz2*, and *Cd68* (Figures S4B and S4C). Given recent findings describing these subsets as immuno-myoblasts in regenerating muscle [26, 28], we hypothesized that these clusters represent MuSC targeted for immune-mediated clearance. Consequently, we excluded these populations from our analysis and re-clustered the remaining four subtypes based on their transcriptional profiles (Figures 4A, S4D and S4E).

Our analysis delineated two distinct clusters of quiescent MuSC (clusters 0 and 1), both characterized by the expression of *Pax7* and *Myf5*, while lacking *Myod1* and *Myog* expression (Figures 4B and S4E). Notably, cluster 0 exhibited a marked enrichment of *Runx1* (Figure S4E), indicating that cells from this cluster are the most quiescent. Moreover, we identified an activated MuSC subcluster (cluster 2)

distinguished by the additional expression of *Myod1* and the proliferation marker *Mki67* (Figures 4B and S4E). Importantly, a fully committed myogenic cell population (cluster 3), characterized by *Myog* expression as well as that of *Mymk* and *Mymx,* and originally absent in control individuals, emerged in mutant mice (Figures 4B and S4E-S4F). In line with this observation, we found that *Ar* expression was confined to quiescent clusters 0 and 1 in control mice, whereas ectopic *Myf5* and *Myod1* expression was noted in cluster 1 in $AR^{(i)sat-/Y}$ individuals (Figure 4B), indicating that loss of AR in MuSC promotes myogenic commitment. Notably, several genes associated with symmetric division, including *Bmi1*, *Msi2*, and *Zfx*, were upregulated in mutant mice within cluster 3 (Figure S4G), alongside a broader expression of the fusogenic markers *Mymk* and *Mymx* across a larger subset of cells (Figure S4F), indicative of symmetric differentiation.

To provide evidence of commitment defaults caused by loss of AR in MuSC, we assessed cell cycle distribution within each cluster (Figures 4C and S4H). Our analysis revealed various perturbations upon AR loss, including cells in G2/M in cluster 1 (Figure 4C). Moreover, in the fully committed cluster 3, the proportion of cells in G1 dropped from ~80% in controls to ~60% in mutants, whereas those in S phase, absent in control mice, increased by more than 15% in MuSC-AR deficient mice (Figure 4C), indicating that they are more prone to mitotic activity.

To investigate the division modalities of MuSC, we performed a series of immunofluorescence analyses. Double staining for PAX7 and KI67 in injured TA muscles from control and $AR^{(i)sat-/Y}$ mice at 5 and 7 dpi revealed a significant reduction in proliferating MuSC in mutant mice (Figures 4D-4F), indicative of impaired symmetric stem cell divisions. Furthermore, double immunodetection of PAX7 and MYOG at 5 dpi showed a marked increase in $PAX7^+/MYOG^+$ cells, accompanied by a decrease in $PAX7^+/MYOG^-$ cells upon AR loss in MuSC (Figures 4G and 4H). By 7 dpi, both $PAX7^+/MYOG^+$ and $PAX7^-/MYOG^+$ cell populations exhibited a twofold increase in $AR^{(i)sat-/Y}$ mice (Figures 4G and 4I), further indicating a shift to symmetric differentiation. Consistently, $MYOG^+/MKI67^+$ cells were detected within regenerating tissue of mutant mice (Figure S4I), in line with our scRNA-seq data indicating an increased proportion of the committed cluster 3, which is characterized by *Mki67* expression in mutants (Figure S4J). Collectively, our findings indicate that AR loss skews MuSC toward symmetric differentiation at the expense of self-renewal (Figure 4N).

We henceforth hypothesized that increased symmetric differentiation may deplete the stem cell pool, compromising its ability to support effective repair during subsequent regenerative challenges. To test this, we subjected control and $AR^{(i)sat-/Y}$ muscles to a secondary CTX-induced injury 28 days after the primary injury, and assessed tissue morphology 7 days later (28+7 dpi). At this stage, control muscles exhibited an accelerated regenerative response compared to muscles analyzed at 7 dpi following a single injury (Figure 4J), consistent with previous reports [1, 29], reflecting a primed regenerative state.

This response was characterized by reduced immune cell infiltration (Figure 4J, cyan arrows), a predominance of centrally nucleated myofibers (Figure 4J, black arrows), and minimal interstitial matrix deposition (Figure 4J, green arrows). In contrast, $AR^{(i)sat-/Y}$ muscles displayed exacerbated pathological features, including persistent immune infiltration (Figure 4J, cyan arrows), multinucleated fibers with pronounced morphological abnormalities, and disorganized fibers with fusion defects and nuclear mislocalization throughout the sarcoplasm (Figure 4J, pink arrows), together with fat deposition (Figure 4J, red arrows). Immunolabeling for DMD further confirmed the structural heterogeneity and irregularities in $AR^{(i)sat-/Y}$ muscles at 28+7 dpi (Figure 4K). These defects were accompanied a threefold reduction in MuSC numbers in $AR^{(i)sat-/Y}$ mice compared to controls as revealed by quantification PAX7-positive MuSC at 28+7 dpi (Figure 4L).

Overall, AR signaling at puberty in MuSC acts as a pivotal regulator of stem cell fate decisions, promoting symmetric divisions to preserve the quiescent stem cell pool, while facilitating asymmetric divisions to ensure timely myogenic differentiation and restoration of injured muscle (Figure 4M). By maintaining this equilibrium between self-renewal and differentiation, AR safeguards both the long-term stem cell reservoir and the efficiency of regenerative responses across repeated injury events.

AR controls MuSC fate through early chromatin remodeling

To capture early AR-dependent chromatin events with the potential to drive the scRNA-seq-detected transcriptomic alterations and downstream regenerative defects, we performed CUT&RUN profiling of AR and the active chromatin mark H3K4me2 in young FACS-isolated MuSC at 5 dpi. Consistent with our observations at 7 dpi, CUT&RUN analysis at 5 dpi identified 7,612 AR binding peaks, primarily localized to intronic and intergenic regions (Figure S5A), associated with 7,040 genes. The majority of these AR-bound loci coincided with H3K4me2 enrichment at promoter regions (Figures S5B and S5C). Motif analysis using HOMER revealed that 50.6% of AR peaks contained canonical AR binding motifs (Figure 5A), confirming the specificity of AR-DNA interactions. Functional enrichment analysis of AR target genes demonstrated significant involvement in pathways critical for stem cell homeostasis and tissue remodeling, notably the HIPPO and PI3K-Akt signaling pathways (Figure 5B). similar to what we described at day 7, gene-centric analysis revealed that AR is mainly recruited within a 100-kb window of more than 50% of differentially expressed genes (Figures 5C and 5D). Representative AR binding loci at key genes involved in these regulatory pathways, including *Clock*, *Eifd2* and *Psma4*, are depicted in Figure 5E. Together, these findings demonstrate that AR engages early with the MuSC chromatin landscape, preferentially at distal regulatory elements enriched in active histone marks, to control the transcriptional programs governing stem cell fate and tissue remodeling.

AR dynamically repositions upon injury to govern time-dependent regenerative genomic programs

The transcriptomic discrepancies observed between 5 and 7 dpi led us to question AR positioning on the DNA during muscle repair. Deeptools analysis demonstrated minimal overlap and distinct peak profiles for each state between AR-bound chromatin landscapes 0- (Basal), 5- and 7 dpi (Figures 5F-5H). This temporal specificity was further confirmed by comparative analysis of the genes bound by AR in those specific clusters (Figure 5F). The genes commonly controlled by AR during the regeneration process were mainly implicated in cell-cell adhesion or in the connection with the synapse, essentially *via* cadherins (e.g. *Cdh2*, *Cdh6*, *Cdh7*), and included *Ar* itself, and *Gli3* that is essential for MuSC injury memory [30] (Figure 5G). More importantly, in the absence of injury, AR binding was enriched at genomic loci associated with MuSC stemness, including *Pax3*, *Pax7*, and *Kdm1a* (*Lsd1*) (Figures 5G and 5H), while AR-bound landscape profile markedly shifted at 5 dpi, targeting genes implicated in MuSC activation, such as *Myf5* and *Tead1*, and asymmetric division like *Aurkb*, or muscle commitment including *Myh4* and *Myh9* (Figures 5G and 5H). 7 dpi, AR was further reallocated to loci related to myogenic differentiation such as *Myod1*, *Mef2a* and *Mef2d*, and asymmetric division like *Numb* and *Pard3* (Figures 5G and 5H). Representative genes exhibiting AR binding loci in a temporal and stage-specific manner during regeneration such as *Pax7*, *Myf5*, and *Myod1* are depicted in Figure 5H. Collectively, these findings reveal that AR is dynamically repositioned in MuSC following injury, engaging stage-specific genomic loci to orchestrate transcriptional programs that govern activation and lineage commitment via MRFs (Figure 5I). This temporal chromatin remodeling ensures a balanced stem-to-committed transition, safeguarding the MuSC pool for future regenerative demands at puberty.

Age-related regenerative decline in skeletal muscle is causally linked to diminished androgen signaling

Since aging is characterized by a progressive decline in MuSC number and skeletal muscle regenerative capacities, we next investigated whether these impairments are dependent on androgen signaling. We thus quantified serum testosterone levels in mice at different ages and observed a progressive decrease from ~25 nmol/L at 2 months of age to a plateau of ~5 nmol/L by 21 months of age (hereafter old mice) (Figure 6A). This was accompanied by a corresponding decrease in *Ar* expression at both the transcript and protein levels in non-injured (NI) TA muscle of old mice compared to young ones (3-month-old) (Figures 6B-6D). Notably, the transcript levels of the MuSC marker *Pax7* were diminished in NI TA of old control mice (Figures 6E and S6H, respectively), suggesting compromised stem cell functionality. We then established that old male mice show markedly impaired regenerative capacity compared to young littermates (3-month-old) after cardiotoxin (CTX)-induced injury TA muscle (Figure

S6A), in agreement with previous reports [10, 11]. 7 dpi, aged control muscles displayed increased interstitial space, sustained immune infiltration, and misshaped regenerating fibers (Figure 6F). Ultrastructural analysis confirmed these impairments, showing disrupted sarcomere organization, fragmented Z-lines, and increased extracellular matrix deposition (Figures 6G and S6B). These structural impairments were accompanied by a significant decrease in MuSC numbers (Figure 6H and 6I), and deformed regenerating fibers (Figure 6J). Consistently, AR expression itself was markedly reduced in PAX7-positive MuSC (Figure S6C). Notably, this recovery was accompanied by a pronounced shift toward oxidative metabolism (Figure 6K), as well as increased fibrosis (Figures 6L and 6M) and adipocyte emergence (Figure 6N), highlighting the pivotal role of AR signaling in safeguarding the structural and functional fidelity of regenerating muscle. Importantly, these phenotypes were further exacerbated in aged AR-deficient mice (Figures 6F-6N), indicating that hormonal decline and receptor loss produce overlapping yet partly distinct defects.

To determine whether the regenerative impairment is causally linked to androgenic insufficiency, we tested whether restoring androgen signaling could reverse aspects of the aged phenotype. We thereby supplemented old mice with 5-α-dihydrotestosterone (DHT) implants. At 7 dpi, DHT-treated mice exhibited significantly improved muscle regeneration, as evidenced by reduced immune infiltration, improved myofiber morphology, and an increased number of nuclei per regenerating fiber (Figures 6O and 6P). Together, these findings provide direct evidence that age-related androgen deficiency causally contributes to impaired aging skeletal muscle regeneration.

Androgen signaling orchestrates distinct gene networks in young and old individuals leading to similar phenotypes

Next, we compared the transcriptomic profiles of old control MuSC to those of young counterparts, and revealed 1,709 differentially expressed genes, including 798 downregulated and 911 upregulated transcripts (Figures 7A and S7A). Pathway enrichment analyses of the downregulated gene set highlighted a significant suppression of pathways related to protein synthesis and peptide/amide metabolism (Figure 7B), suggesting a reduced biosynthetic capacity in aging MuSC. Notably, several genes essential for myogenic differentiation and structural regeneration were significantly downregulated. These included *Myh4* and *Myod1* in addition to genes involved in sarcomere organization and contractile function, such as nebulin (*Neb*), *Tpm3*, and troponin C type 2 (*Tnnc2*) (Figures 7A and 7C). This transcriptional repression is consistent with the defective regenerative phenotype and histological and ultrastructural impairments observed in aged control mice at 7 dpi. Conversely, pathway analyses on the 911 genes upregulated in MuSC from old control mice compared to young control counterparts, revealed that these genes were predominantly associated with

metabolic and biosynthetic processes, notably the regulation of RNA, microRNA, nitrogen metabolism, and nucleobase-containing compound metabolic pathways (Figures 7A and 7B), but also oxidative metabolism processes (e.g. *Acadsb*, *Coq8b, Coq10b* and *Pdk4*) (Figures 7A and 7C), collectively indicating a metabolic transition toward oxidative phosphorylation in old MuSC. These molecular findings align with the histological evidence of enhanced oxidative metabolism observed at 7 dpi in old individuals. Remarkably, a substantial fraction of differentially expressed genes in old mice also exhibited AR binding within 100 kb of their TSSs (Figure 7D). However, the majority of AR-responsive genes identified in young mutant mice were not recapitulated by aging process (Figure 7E), even though gene ontology analysis revealed similar functional enrichment (Figures S7B-S7E). This limited convergence highlights that, while AR deficiency in MuSC at puberty mimics certain transcriptional features of aging, the molecular underpinnings differ, reflecting the distinct role of AR during pubertal development as opposed to the combined decline of hormone and receptor signaling observed in the elderly. Altogether, these findings support a model in which AR orchestrates regenerative transcriptional programs in MuSC *via* enhancer-driven mechanisms, a regulatory framework that persists with age but becomes functionally altered.

To extend our findings to a human model, we determined AR expression in LHCN-M2 and C79 myoblasts, isolated from young and aged male individuals, respectively. Notably, AR expression was reduced by approximately 50% in C79 compared to LHCN-M2 myoblasts at both the transcript (Figure 7F) and protein levels (Figures 7G and 7H), in addition to the PAX7 levels (Figure 7I). Moreover, LHCN-M2 cells displayed a higher propensity for proliferation (Figures 7J and S7I) and differentiation compared to C79 cells (Figure 7K), mirroring the differences observed between young and aged mice. In agreement, AR knockdown in both cell lines strongly impaired differentiation, as indicated by the conservation of a fibroblast-like morphology, and lack of the characteristic spindle-shaped structure observed in control cells, 5 days post-differentiation (dpd) (Figures 7K, S7J and S7K). Collectively, these findings demonstrate that intact AR signaling, requiring both sufficient ligand and receptor, is essential for efficient myoblast differentiation, and by extension, effective skeletal muscle regeneration.

DISCUSSION

Maintenance of the MuSC reservoir requires mechanisms that preserve quiescence, while ensuring that repair proceeds with structural and functional fidelity. In male skeletal muscle at puberty, AR expression concentrates in the most quiescent, self-renewing MuSC states, and is largely extinguished as cells commit. Conditional loss of AR in MuSC disrupts dormancy, accelerates cell-cycle entry, and drives symmetric differentiation on the expense of stem cells renewal, leading to attrition of the regenerative pool. On this basis, we here identify AR as lineage-intrinsic indicator of MuSC stemness in males, functionally distinct from its canonical anabolic role in myofibers [15, 24, 25, 31].

This AR-stemness relationship fits within a broader endocrine framework across the male life course. At puberty, androgens promote the establishment of a long-lived quiescent MuSC pool from juvenile precursors through a Notch-dependent pathway [17]. With aging, declining systemic androgens correlate with reduced MuSC number and impaired repair [32], and androgen supplementation restores regenerative capacity in low-androgen settings [33, 34]. Consistent with this trajectory, our MuSC-specific AR knockout phenotypically recapitulates features of aging-associated stem cell exhaustion, including reduced responsiveness to repeated injuries, suggesting that androgen decline and diminished AR activity converge on shared mechanisms that erode the MuSC reservoir. It is worth noting, however, that transcriptomic differences observed between AR-deficient young MuSC and those from aged controls may also reflect distinct underlying causes, namely, the selective inactivation of AR in otherwise intact young MuSC versus the broader loss of stem cells with age, along with age-related alterations in the muscle microenvironment [35]. These observations indicate that androgen decline and AR loss exert distinct yet complementary effects, the former reduces stem cell abundance and responsiveness, while the latter disrupts intrinsic programs of quiescence and fate. In aged AR-deficient mutants, these deficits appear to sum, producing an exacerbated phenotype that underscores the dual contribution of hormone and receptor to MuSC maintenance.

We also observe that AR expression at puberty persists for weeks after injury in MuSC derived from self-renewal, reflecting early symmetric divisions driven by AR that maintain the quiescent stem pool for future regenerative demands. In contrast, differentiating MuSC gradually lose AR, showing that AR not only supports stem cell expansion, but also controls asymmetric divisions to produce committed cells for repair. Without AR, MuSC divisions favor committed daughters over self-renewal, depleting the reserve and impairing regeneration after repeated injury. This AR-dependent balance between renewal and differentiation in male MuSC has not been shown *in vivo* before. Earlier studies using female-derived C2C12 myoblasts showed DHT enhances proliferation, but these cells lack true quiescence and do not represent adult male muscle stem cells [19, 36, 37]. In contrast, our findings reveal

that physiological androgen levels *via* AR in male MuSC dynamically regulates their fate during regeneration.

MuSC-AR influences more than lineage fate in skeletal muscle. It promotes proliferation and differentiation in myogenic cells [38, 39], and its loss in our mouse model leads to fusion defects, fiber orientation defaults, and impaired ultrastructure, reflecting not only reduced progenitor output, but also a disrupted regenerative program in these progenitors. This contradicts earlier claims that MuSC-AR is dispensable for regeneration (Sakai et al., 2020), likely because their model did not disrupt AR in the early, true stem MuSC population. Our data clearly establish MuSC-intrinsic AR as a crucial regulator of androgen-driven muscle repair in males. This signaling axis also shapes metabolic identity. While myofiber-AR supports glycolytic metabolism, its absence in MuSC at puberty shifts regenerated fibers toward oxidative pathways, which was recapitulated in aged individuals. Seahorse assays and histology confirm this shift, consistent with findings in AR-deficient myofibers [24, 40], AR-related disorders [41], and aging muscle [42, 43]. Notably, myofiber-AR loss is linked to increased β-oxidation gene expression and reduced Complex IV components [24, 44], though this latter feature was absent in our model, possibly due to reactive oxygen species accumulation impairing electron transport and causing mitochondrial stress [45].

At the tissue level, MuSC-AR deletion at puberty reveals increased inflammation, fibrosis, and adipocyte accumulation at the site of injury. Similar disturbances occur in androgen-deprived states, where impaired inflammatory resolution and accelerated fibro-adipogenic drift are observed [46, 47]. These findings show that MuSC are not passive recipients, but active transmitters of androgen-sensitive signals shaping their microenvironment. This supports a bidirectional model in which AR in MuSC governs intrinsic fate decisions while orchestrating stromal and immune crosstalk during muscle repair.

To coordinate these diverse, stage-specific functions during muscle regeneration, we propose a dynamic chromatin occupancy model in which AR sequentially engages distinct transcriptional programs as MuSC progress from quiescence through activation to commitment. Such nuclear receptor mobility and partner switching are well documented in other systems [48-51]. Emerging evidence in skeletal muscle shows AR collaborates with SMAD signaling to enhance BMP-driven transcriptional programs that regulate muscle mass and quality [52]. In aging and pathological expansions of the AR-polyglutamine tract, altered chromatin binding and disrupted co-factor interactions have been observed [53, 54], suggesting that reduced AR availability with age may limit its genomic sampling and assembly of stage-specific complexes necessary to maintain stemness, and sequentially enable differentiation.

In sum, MuSC-AR preserves quiescence, sustains the stem cell pool, shapes glycolytic identity, and orchestrates niche remodeling. Its decline leads to reserve loss, metabolic drift, and regenerative failure (Figure S7L), highlighting MuSC-AR as a therapeutic target in aging and disease.

METHODS

Mouse Studies

Housing

Mice were maintained on a C57BL/6 background and housed in a temperature- and humidity-controlled facility under a 12-hour light/dark cycle, with *ad libitum* access to standard rodent chow (2800 kcal/kg, Usine d'Alimentation Rationelle, Villemoisson-sur-Orge, France) and water. Breeding and maintenance followed institutional guidelines, and all experiments were conducted in an accredited facility in compliance with French and EU regulations on laboratory animal use (Directive 2010/63/EU). Procedures were approved by the local ethical committee (Com'Eth, Strasbourg, France) and by the French Ministry of Research (MESR). Mice were euthanized *via* cervical dislocation, and muscles were harvested for histological and molecular analysis.

Generation of $AR^{(i)sat-/Y}$ mutant mice

For satellite cell-specific androgen receptor (AR) ablation, $AR^{L2/L2}$ female mice, carrying LoxP sites flanking chromosome X exon 1 encoding the AR N-terminal domain [55], were intercrossed with *Pax7*-$CreER^{T2}$ male mice [56] to generate *Pax7*-$CreER^{T2}/AR^{L2/Y}$ mice, which express $CreER^{T2}$ recombinase selectively in satellite cells. To induce recombination, 9-week-old $AR^{L2/Y}$ control males and their *Pax7*-$CreER^{T2}/AR^{L2/Y}$ pre-mutant littermates received intraperitoneal tamoxifen injections (1 mg/mouse/day) for five consecutive days, generating control and $AR^{(i)sat-/Y}$ mutant mice. Alternatively, mice were intercrossed with a *Rosa26*-YFP reporter line [57] to generate *Pax7*-$CreER^{T2}/AR^{L2/Y}$/*Rosa26*-$YFP^{Tg/0}$ mice with one YFP allele, allowing selective labeling of satellite cells and lineage tracing of their progeny. Primer sequences required for genotyping PCR are listed in Supplementary Table 1.

Mouse Treatments

For cardiotoxin-induced muscle injury model, mice were anesthetized with 2.5% isoflurane using a SomnoSuite device. To induce muscle damage, 20 µl of 25 µM cardiotoxin (CTX) (Latoxan, Valence, France, L8102), dissolved in phosphate-buffered saline (PBS) were injected into the tibialis anterior (TA) muscle.

For androgen supplementation, 5-alpha-dehydrotestosterone (DHT) implants were inserted subcutaneously in the intrascapular region of 21-month-old wild-type male mice, as described [58]. Muscle injury was induced by CTX injection three weeks post-implantation to avoid off-target effects caused by DHT-burst.

Testosterone serum levels measurement

Blood was collected from mice in 50 mM EDTA tubes (Sigma-Aldrich), and plasma was isolated by centrifugation at 3,000 g for 15 minutes at 4°C. The supernatant was collected, and serum testosterone levels were quantified using the Testosterone Rat/Mouse ELISA Kit (LDN, AR E-8000R), following the manufacturer's instructions.

Contractile Measurements

In situ isometric TA muscle force in response to nerve stimulation was measured as described [25]. In brief, specific maximal tetanic force (mN/mm^2) was determined by dividing the measured force by the estimated CSA of the muscle. Assuming a cylindrical muscle shape with a density of 1.06 mg/mm^3, the CSA was calculated as the volume of the muscle divided by its (muscle) length. The optimal muscle length (L0) was defined as the length at which maximal tetanic force was observed. All data collected from the muscle lever system were recorded and analyzed using a microcomputer with the PowerLab/4SP system (AD Instruments).

Histological analyses

Muscle histology

Muscles were either snap-frozen in liquid nitrogen-cooled isopentane for cryosections, or fixed in 4% PFA overnight at 4 °C then washed in PBS and 70% ethanol and embedded in paraffin. 10 µm thick cryosections were prepared at −20 °C using a 2800 Frigocut cryostat (Leica, St Jouarre, France) and kept at −20 °C until further analysis. 5 µm thick paraffin sections were cut at room temperature (RT) using a microtome (Leica RM, 2145, 0737/09.1998) and stored at 4 °C until further analysis.

Hematoxylin and eosin, and Masson's Trichrome staining were performed on paraffin sections as described, while NADH and COX staining were assessed on cryo-sections as described [24, 57, 59].

Quantification of Collagen Deposition

Collagen content assessed by Sirius Red staining (Picro-Sirius Red Stain, Pint, StatLab, STPSRPT) was imaged under a bright-field microscope, or under polarized light using the Axioscan 7 (Carl Zeiss) slide scanner. Birefringent collagen fibers were visualized based on their differential light refraction properties, allowing for the selective detection of collagen deposition. Quantification was performed by analyzing the polarized signal intensity and distribution across the tissue using standardized image analysis parameters established by the in-house anatomic pathology platform.

Immunofluorescence staining

Paraffin and cryo-sections were processed using distinct protocols tailored to antibody requirements. Paraffin sections underwent deparaffinization, and antigen retrieval was done under controlled temperature and pressure conditions for 20 min in either tris-hydroxymethyl-aminomethane (Tris buffer) (pH=9.0) or in Signal Stain ® Citrate Unmasking Solution (Cell Signalling 14746S). In contrast, frozen sections were fixed for 10 min in 4% PFA at RT, and permeabilized with PBST for 15 min at RT. Afterwards, paraffin or frozen sections were incubated overnight at 4 °C with the primary antibodies diluted in PBST directed against AR (Rabbit, Abcam, ab108341, 1:500), PAX7 (Rabbit; Thermo Fisher, PA1-117, 1:400, or Mouse; DSHB, AB_528428, 1:50), MYOG (Abcam, ab1835, 1:400), ACTN1 (Mouse, Abcam, ab9465, 1:400), DMD (Mouse, IGBMC , 1Dystro1D2, 1:1000 or Rabbit sigma, D8168, 1:400), KI67 (Rat, R&D systems, 14-5698-82, 1:500), LAMA2 (Rat, Sigma Aldrich, L0663-.1ML, 1:500), eMyHC (Mouse, DSHB, F1.652, 1:20), F4/80 (Rabbit, Cell Signaling, 70076, 1:400) and PLIN1 (Rabbit, Abcam, Ab3526. 1:200). Mouse (Santa Cruz Biotechnology, E3117, 1:500), rat (Vector Laboratories, BA-4000, 1:500) or rabbit (PeproTech, 500-P000-500UG, 1:500). IgGs were used as controls. Sections were rinsed with wash buffer, and incubated with appropriate Alexa-Fluor-conjugated secondary antibodies with different fluorescent wavelengths (488, 555 or 647 nm, 1:500, Invitrogen: a32732, a32723, a21206, a21424, a48265, a32733, a32728) in permeabilization buffer for 45 min at RT. After wash, slides were mounted with Fluoromount™ Aqueous Mounting medium containing DAPI (Invitrogen, 00-4959-52).

Fiber cross-sectional area measurements

Muscle cross-sections were stained with DMD (Abcam, ab15277, 1:500) mark the sarcolemma surrounding each fiber. CSAs were quantified using QuPath (open-source image analysis software) integrated with a customized Groovy macro (available via GitLab). In brief, individual fibers were identified based on the intensity and continuity of the stained sarcolemma surrounding each fiber by segmentation. Areas were measured after background subtraction and automated thresholding.

Muscle ultrastructural analysis

1 mm^2 TA muscle samples were fixed overnight at 4°C by immersion in a mix of 2.5% glutaraldehyde and 2.5% paraformaldehyde diluted in 0.1 M cacodylate buffer (pH 7.4), washed in the same buffer for 30 min, and stored at 4°C. Post-fixation was performed with 1% osmium tetroxide in 0.1 M cacodylate buffer for 1 h at 4°C, followed by dehydration through a graded ethanol series (50%, 70%, 90%, and 100%) and propylene oxide (30 min each). Samples were oriented longitudinally or transversally and embedded in Epon 812. 70 nm ultrathin sections were obtained and contrasted with

uranyl acetate and lead citrate. Imaging was performed at 70 kV using a Morgagni 268D electron microscope, with digital acquisition via a Mega View III camera (Soft Imaging System).

Cell culture analyses

Cell culture and treatments

LHCN-M2 and C79 cells were cultured in Dulbecco's Modified Eagle Medium (DMEM 4,5 g/L of glucose, Invitrogen 4165-062)/Medium 199 (Invitrogen 22340-020) (4:1), supplemented with 20% fetal calf serum (FCS), 25 µg/mL fetuin, 5 µg/mL human insulin, 40 µg/mL gentamycin and 0.5 ng/mL basic fibroblast growth factor (bFGF) along with 5 ng/mL human epidermal growth factor (hEGF) and 0.2 µg/mL dexamethasone [60]. Cells were maintained at 37°C in a humidified atmosphere with 5% CO_2. Cells were split at 70-80% confluence, and the medium was replaced every 48 hours.

To induce differentiation, LHCN-M2 and C79 cells were seeded at 90% confluence and switched at confluence to differentiation medium (DMEM supplemented with 2% horse serum and 40 µg/mL gentamycin) for up to 5 days, with medium changes every 48 hours.

For transfection, human AR siRNA (5'- GGGCACTTCGACCATTTCTGA-3'), or scramble siRNA (5'-AAGCTTCATAAGGCGCATAGC-3'), were introduced using Typical RNAiMAX Transfection kit (ThermoFischer, 13778075), following the manufacturer's protocol. Cells were seeded in six-well plate and transfected with 50 nM siRNA diluted in Opti-MEM (Gibco, USA) at 50–60% confluence for 24 h, after which the medium was replaced with fresh differentiation or growth medium. Cells were subsequently treated with 100 nM of DHT (Sigma, A8380-1G) diluted in ethanol 24 h after transfections.

Cell Proliferation Analysis

Cell proliferation was assessed using the CellTrace™ CFSE (Carboxyfluorescein Succinimidyl Ester) Assay (Thermo Fisher Scientific, USA, C34557) as described [61]. Briefly, LHCNM2 and C79 cells were incubated with 5 µM CFSE at 37°C for 20 min in a humidified atmosphere with 5% CO_2. The labeling reaction was quenched by adding an equal volume of complete growth medium, followed by two washes with PBS to remove excess dye. Labeled cells were kept in appropriate culture conditions and collected at 24-, 48-, and 72-hours post-labeling for flow cytometry analysis. CFSE fluorescence intensity was measured using a flow cytometer (BD LSRFortessa™, BD Biosciences, USA) with excitation at 488 nm and emission detection at 530 nm. Data were analyzed using FlowJo software (BD Biosciences, USA), and cell proliferation was determined by monitoring the progressive dilution of CFSE fluorescence across multiple cell generations. To identify non- and slow-proliferating cells, we

defined the 30% of cells exhibiting the highest CellTrace Violet signal in control as the reference population, and calculated the proportion of cells with equal or greater signal intensity.

Immunocytochemistry

Immunocytofluorescence assay was performed by incubating fixed LHCN-M2 and C79 cells with AR (Rabbit, Abcam, ab108341, 1:500) and PAX7 (Mouse; DSHB, AB_528428, 1:50) antibodies. Observations were made under a Leica confocal microscope.

Seahorse analysis of LHCN-M2 myoblasts

Mitochondrial respiration was assessed using the Seahorse XF Cell Mito Stress Test Kit (Agilent Technologies, Part Number: 103015-100) according to the manufacturer's protocol. Briefly, ~1800 LHCN-M2 myoblasts were seeded in Seahorse XF cell culture microplates (Agilent), and treated with either vehicle or 100 nM flutamide (Abcam, ab141234) for 1 hour. The assay was performed on a Seahorse XFe96 Analyzer (Agilent), following the sequential injection of oligomycin (1 µM), FCCP (2.5 µM), and rotenone/antimycin A (1 µM). Basal respiration, ATP-linked respiration, maximal respiration, and spare respiratory capacity were calculated using Wave software (Agilent).

Flow cytometry analysis

Muscle cell populations composition

Muscle stromal vascular fraction was isolated as described [62]. Briefly, hind limb muscles were dissected, minced into small fragments, and enzymatically digested with 1.25 U/mL Dispase II (Stemcell Technologies, Cat: 07913) and 500 µg/mL Collagenase Type I (Thermo Fisher Scientific, 17018029). The resulting cell suspension was sequentially filtered through 100 µm, 70 µm, and 40 µm cell strainers (Corning Life Sciences) to remove debris. Cells isolated from digested muscle tissue were stained with CD45 Alexa eFluor700 (eBioscience, 56-0451-82, 1:100), CD31 PE (eBioscience, 12-0311-82, 1:100), SCA-1 PE-Cy7 (eBioscience, 25-5981-82, 1:100), and Integrin-α7 (ITGA7) FITC (MBL, K0046-4, 1:50). Cells were analyzed based on forward scatter (FSC) and side scatter (SSC) parameters to exclude debris and doublets. CD45- and CD31-positive cells were quantified to assess immune and endothelial cell populations, respectively. After removing CD45/CD31-expressing cells, SCA-1-positive cells were gated to identify fibro-adipogenic progenitor cells (FAPs). Finally, SCA-1-negative, ITGA7-positive cells were classified as satellite cells. Fluorescence intensity was measured using a flow cytometer (BD FACSymphony A1™, BD Biosciences, USA). Analysis were conducted using FlowJO software as described [62].

Muscle immune cell populations composition

Cells isolated from digested muscle tissue were stained with CD45 Alexa eFluor700 (eBioscience, 56-0451-82, 1:100), CD11b PerCP-Cy5.5 (BioLegend, 101228, 1:100), Ly-6G-GR-1 FITC 488 (BioLegend, 108417, 1:100), Ly-6C PE-CF594 (BD Horizon™, AB_2737749, 1:100), F4/80 APC eFluor 780 (eBioscience™, 47-4801-82, 1:100), CD19 BUV 737 (BD Horizon™, AB_2870087, 1:100), and CD206 BUV 785 (BioLegend, 321142, 1:100). Cells were analyzed based on forward scatter (FSC) and side scatter (SSC) parameters to exclude debris and doublets. Data analysis was performed by sequential gating on single, live $CD45^+$ leukocytes, followed by identification of myeloid cells as $CD11b^+$, neutrophils as $CD11b^+Ly6G^+$, monocytes as $CD11b^+Ly6G^-Ly6C^+$, and macrophages as $CD11b^+Ly6G^-Ly6C^-F4/80^+$, with M2-like macrophages defined as $CD11b^+F4/80^+CD206^+$. B cells were identified as $CD19^+$ within the $CD45^+$ population. Fluorescence intensity was measured using a flow cytometer (BD FACSymphony A1™, BD Biosciences, USA). Analyses were conducted using FlowJO software.

Fluorescence-Activated Cell Sorting (FACS) of Satellite Cells

After stromal vascular fraction isolation, mononucleated cells were pelleted by centrifugation at 400g for 5 min, resuspended in FACS buffer (DMEM without phenol red, 4.5 g/L glucose, 2% BSA, 2 mM EDTA), and labeled with fluorescence-conjugated antibodies. Cells were stained with CD45 PE (eBioscience, 12-0451-83, 1:100), CD11b PE-Cy7 (eBioscience, 25-0112-82, 1:100), CD31 PE (eBioscience, 12-0311-82, 1:100), TER119 PE (BD Pharmingen™, 553673, 1:100), ITGA7 FITC (MBL, K0046-4, 1:50), CXCR4 APC (eBioscience, 17-9991-82, 1:100), and CD34 eFluor405 (eBioscience, 48-0341-82, 1:33). Cells were gated based on FSC and SSC parameters to exclude cellular debris and doublets. Leukocytes and endothelial cells were removed by gating out CD45-, CD11b-, CD31-, and TER119-positive populations. The remaining fraction was further gated for CD34 and ITGA7 expression, and double-positive cells were selected based on CXCR4 expression. Fluorescence intensity and sorting were conducted using a FACS sorter (BD FACSAria™, BD Biosciences, USA). Sorted satellite cells were subsequently processed for RNA extraction or CUT&RUN analyses.

CUT&RUN Assay and Bioinformatics Analysis

CUT&RUN was performed as described [62, 63]. Briefly, FACS-isolated satellite cells were centrifuged at 500 g for 10 min at 4°C, and the resulting cell pellet was incubated with nuclear extraction buffer (20mM HEPES-KOH pH = 7.9, 10 mM KCl, 0.5 mM Spermidine, 0.1% Triton X-100, 20% Glycerol and protease inhibitor cocktail) for 20 min on ice. Isolated nuclei were then washed and incubated with Concanavalin A-coated beads (BioMag Plus Concanavalin A, Cat: 86057-3) for 10 min at 4°C. Following additional washes, the nuclei-bead complexes were incubated overnight at 4°C with gentle agitation

in the presence of primary antibodies targeting AR (Abcam, ab108341, 1:100) and H3K4me2 (Active Motif, 39141, 1:100), and a Rabbit IgG (PeproTech, 500-P000-500UG, 1:100). Nuclei-bead complexes were precipitated and incubated with protein A-micrococcal nuclease (pA-MN, IGBMC) for 1 h at 4°C under constant agitation. Enzymatic cleavage was initiated by adding 3 µL of 100 mM $CaCl_2$, followed by 30 min of incubation on ice. The reaction was terminated at 37°C for 20 min using stop buffer (200 mM NaCl, 20 mM EDTA, 4 mM EGTA, 50 µg/mL RNase A, 40 µg/mL glycogen, 25 pg/mL yeast spike-in DNA). DNA was extracted from immunoprecipitated samples for sequencing. Libraries were generated from immunoprecipitated DNA as described [62], and sequenced on an Illumina HiSeq 2000 platform. Reads overlapping ENCODE blacklist regions (V2) were removed, and deduplicated unique reads were conserved for further analysis. Reads were mapped to the mm10 reference genome using Bowtie2 (v2.3.4.3) [64]. To generate genome-wide intensity profiles, uniquely mapped reads were processed as follows: Bigwig files were generated using bamCoverage (deeptools 3.3.0) [65], with normalization by RPKM (--normalizeUsing RPKM --binSize 20). Raw bedgraph files were produced with genomeCoverageBed (bedtools v2.26.0) [66]. Peak calling was performed using SEACR [67] and MACS2 [68] with IgG-immunoprecipitated samples as controls (-keepall), and peaks with an FDR at least less than 0.05 were retained for further analysis. The IGV genome browser (http://software.broadinstitute.org/software/igv/) was used for genome-wide intensity visualization. Peaks were annotated, and motif analysis was conducted using HOMER. Genomic feature distribution (promoters/TSS, 5' UTRs, exons, introns, 3' UTRs, transcription termination sites, and intergenic regions) was determined based on RefSeq and HOMER annotations. For bioinformatics and clustering analysis, Venn diagrams were generated using Venny (2.1.0) (https://bioinfogp.cnb.csic.es/tools/venny/). Clustering analyses were performed using seqMINER [69] and deeptools (-computeMatrix -skip0; -plotHeatmap) with K-Means linear normalization. Genomic intersections and sequence extractions were carried out using bedtools. GetFastaBed was used to extract FASTA sequences from BED files. Intersect Interval and Multiple Intersect were applied to identify overlapping genomic locations. WindowBed was utilized for gene-centric peak distribution analyses. When not specified, all bioinformatics analyses were performed using default parameters, ensuring robust and reproducible results.

RNA extraction and analyses

Total RNA from muscle tissue, LHCN-M2 and C79 cell lines was extracted using TRIzol reagent (TRIREAGENT, Molecular Research Center, TR-118, 513-841-0900) as described [70]. RNA concentration and purity were assessed spectrophotometrically using a NanoDrop system (Thermo Fisher Scientific).

For RNA isolation from FACS-isolated MuSC, the RNeasy Plus Micro Kit (Qiagen, 74034) was employed according to the manufacturer's instructions.

For RT-qPCR experiments, 2 µg of total RNA underwent reverse transcription using SuperScript IV (Life Technologies) with oligo(dT) primers, according to the supplier's protocol. cDNA was diluted hundred times and quantitative PCR (qPCR) was performed with a Lightcycler 480 II (Roche) using the SYBR® Green PCR kit (Roche), in accordance with the recommended protocol (2 µl cDNA, 4.8 µl H_2O, 5 µl Syber Green 2x mix and 0.2 µl of 100 µM primer mix). The primer sequences for mouse and human are detailed in Supplementary Tables 2 and 3, respectively. Housekeeping genes *Tbp* (for mouse), and *HSP90AB1* (for human) were used as internal controls. Data were analyzed using ΔΔCt [71] method.

For RNA sequencing (RNA-seq) and SMART-seq experiments, RNA integrity was assessed using a Bioanalyzer. Library preparation was performed at the GenomEast platform from IGBMC.

For RNA-seq, cDNA library was prepared, and sequenced by the standard Illumina protocol (HiSeq 4000, single-end, 50 bp), following the manufacturer's instructions. Image analysis and base calling were performed using RTA 2.7.7 and bcl2fastq 2.17.1.14. Adapter dimer reads were removed using DimerRemover. FastQC 0.11.2 (http://www.bioinformatics.babraham.ac.uk/projects/fastqc/) was used to evaluate the quality of the sequencing. Reads were mapped to the mouse mm10 genome (NCBI Build 38) using STAR v2.7.10b [72]. Only uniquely aligned reads were retained for further analyses. Quantification of gene expression was performed using HTSeq 0.11.0 [73]. For comparison among datasets, the transcripts with more than 100 raw reads were considered.

For SMART-seq, full length cDNA was generated from 250 pg to 2 ng of total RNA using SMART-Seq® mRNA Kit (Takara Bio Europe, Saint Germain en Laye, France), according to manufacturer's instructions, with 12 cycles of PCR for cDNA amplification by Seq-Amp polymerase. Six hundred pg of pre-amplified cDNA were used as input for Tn5 transposon tagmentation followed by 12 cycles of library amplification using Nextera XT DNA Library Preparation Kit and IDT for Illumina DNA/RNA UD Indexes, Tagmentation (Illumina, San Diego, USA). Following purification with SPRIselect beads (Beckman-Coulter, Villepinte, France), the size and concentration of libraries were assessed using Bioanalyzer 2100 system (Agilent technologies, Les Ulis, France). Libraries were sequenced on an Illumina NextSeq 2000 sequencer as paired-end 50 base reads. Image analysis and base calling were performed using RTA version 2.7.7 and BCL Convert version 3.8.4. Adapter dimer reads were removed with DimerRemover (-a AGATCGGAAGAGCACACGTCTGAACTCCAGTCAC), and the quality of sequencing data was evaluated using FastQC 0.11.5. Reads were aligned to the mouse mm39 genome using STAR v2.7.10b, retaining only uniquely mapped reads for downstream analyses. Gene expression was quantified using STAR, and for dataset comparisons, only transcripts with more than 50 raw reads were considered.

For RNA sequencing (RNA-seq) and SMART-seq experiments, differentially expressed genes (DEGs) were identified using the Bioconductor libraries DESeq2 [74] with a $p < 0.05$. Identified DEGs were subjected to functional analysis using STRING 12.0 [75] and to pathway analysis using WebGestalt [76] with the Over-Representation Analysis (ORA) method, applying a false discovery rate (FDR) < 0.05 as the significance threshold. Heatmaps were generated by centering and normalizing expression values using Cluster 3.0 [77], with subsequent visualization Morpheus (https://software.broadinstitute.org/morpheus/). Genes were clustered using K-Mean with gene tree construction, Pearson correlation, and average linkage as clustering parameters [78].

Single-cell RNA sequencing

Single-cell RNA sequencing (scRNA-seq) experiments were performed on TA muscle cells, isolated from 3 control ($AR^{L2/Y}$) and 3 $AR^{(i)sat-/Y}/YFP^{Tg/0}$ injured TA muscles at 5 dpi. TA muscles were dissociated into single cells, as described above. Cells from each genotype group were pooled and stained with DAPI, and DAPI-negative living cells were isolated using a BD FACS Aria™ Fusion flow cytometer. To assess cell viability and yield, a Trypan blue exclusion assay was performed using a Neubauer Chamber. Only samples with a viability greater than 95% were processed using a Chromium Controller (10X Genomics, Leiden, The Netherlands). 16,500 total cells were loaded per well to yield approximately 10,000 captured cells into nanoliter-scale Gel Beads-in-Emulsion (GEMs). Single cell 3 prime mRNA seq library were generated using Chromium Next GEM Single Cell 3 prime Reagent Kits v3.1 (10X Genomics). Libraries were quantified and controlled for their quality using Bioanalyzer 2100 (Agilent Technologies, Santa Clara CA), and further sequenced on an Illumina NextSeq 550 sequencer as paired-end 28 + 100 base reads. Image analysis and base calling were performed using RTA version 2.7.7 [79] and Cell Ranger version 3.0.2 [80].

Data were processed using the Cell Ranger 7.0.0 count pipeline (10x Genomics) for read alignment, barcode and unique molecular identifier (UMI) filtering, and gene quantification. A custom reference genome was generated using the mkref function with the GRCm39 assembly of the *Mus musculus* genome and Ensembl release 107 annotations. The output gene-barcode matrix was imported into RStudio (version 2025.05.1) using the Read10X function from the Seurat package (version 5), yielding a sparse matrix of UMI counts per gene per cell. Downstream analyses were conducted in RStudio following standard Seurat v5 workflows [81], including quality control, normalization, dimensionality reduction, clustering, and differential gene expression. For quality control, cells with <10% mitochondrial content, <50% ribosomal gene expression, and total RNA features between 200 and 6000 were retained. Principal Component Analysis (PCA, dim=16) was used for dimensionality reduction, and clustering was performed using a resolution parameter of 0.6. Differential gene

expression and further downstream analyses were conducted. Satellite cell reclustering was performed with dimension reduction of 14 and cluster resolution of 0.3.

Cell-cell communication analysis was conducted using the CellChat R package within the RStudio environment [82]. Normalized scRNA-seq data were used, and overexpressed ligands and receptors were identified to infer intercellular signaling networks. Communication probabilities were computed using the trimean method, with a minimum gene expression threshold of 0.1, and genes were considered only if expressed in more than 10% of cells in the described groups. The CellChatDB ligand-receptor interaction database was used as the reference. The analysis pipeline included identification of major signaling inputs and outputs, classification of signaling roles (incoming, outgoing, mediator, and influencer), and visualization via circle plots and hierarchical clustering. Inter-condition comparisons were performed using the compareInteractions and rankNet functions. All analyses were performed using default CellChat parameters, including 500 permutations for significance testing and standard visualization settings, unless otherwise specified. Results were visualized and further interpreted using built-in and custom R scripts. Cell cycle bioinformatic analyses were performed using Scanpy function (scanpy.tl.score_genes_cell_cycle), with marker genes extracted from scRNA-seq of mouse embryonic stem cells generated for DeepCycle as described [81, 83].

Protein analysis

TA muscles were mechanically ground in RIPA buffer [50 mM Tris (pH 7.5), 1% NP-40, 0.5% sodium deoxycholate, 0.1% SDS, 150 mM NaCl, 5 mM EDTA, and a protease inhibitor cocktail (45 mg/ml; Roche, Cat. No. 11 873 580 001)] at 4 °C. Alternatively, adherent cells were harvested in RIPA buffer, and kept on ice for 10 min. TA muscles and cell lysates were centrifuged at 12,000 g for 10 minutes at 4 °C, and the supernatants were collected for further analysis. For western blot analyses, homogenates were separated in 8% polyacrylamide gels, transferred to Hybond nitrocellulose membranes (Amersham Biosciences), and probed with specific antibodies targeting AR (Abcam, ab108341, 1:500), α-TUBULIN (IGBMC, 1Tub2A2, 1:5000), and GAPDH (Cell Signaling, #2118, 1:5000). Secondary antibodies conjugated to horseradish peroxidase (anit-Mouse-HPR, Cell Signalling, 7076S, 1:10,000; anit-Rabbit-HPR, Cell Signalling, 7074S, 1:10,000;) were detected using chemiluminescence detection systems (GE Healthcare, Amersham, ImageQuant 800 or Imager 600). Protein quantification was assessed by the FIJI/ImageJ distribution software (https://imagej.net/ImageJ) [84].

Statistical analyses

Data processing and analysis were conducted using DESEq2, Microsoft Excel and GraphPad Prism 9. In all graphical representations, error bars indicate the standard error mean (SEM). Comparisons

between groups were performed using appropriate statistical tests, selected based on the number of groups, data distribution (normality), variance homogeneity, and multiple comparisons. The specific statistical tests applied are indicated in the figure legends. Statistical significance was defined as follows: ns, $p > 0.05$ (non-significant); *, $p < 0.05$; **, $p < 0.01$; and ***, $p < 0.001$.

DATA AVAILABILITY

Custom macro for CSA measurements and Sirius Red quantification are available on GitLab and GitHub, respectively (CSA: the BIOP cellpose extension guide; Sirius Red: https://github.com/Hugues-Jacobs/Fibrosis_analysis). All sequencing datasets generated in this study have been deposited in the Gene Expression Omnibus (GEO) under the following accession numbers: GSE303611 for single-cell RNA-seq, GSE303612 for SMART-seq, GSE303614 for bulk RNA-seq, GSE303615 for CUT&RUN analysis at 5 dpi, GSE303618 for CUT&RUN analysis at 7 dpi, and GSE303620 for CUT&RUN analysis in non-injured animals.

REFERENCES

1. Charge, S.B. & Rudnicki, M.A. Cellular and molecular regulation of muscle regeneration. *Physiol Rev* **84**, 209-238 (2004).
2. Goel, A.J., Rieder, M.K., Arnold, H.H., Radice, G.L. & Krauss, R.S. Niche Cadherins Control the Quiescence-to-Activation Transition in Muscle Stem Cells. *Cell Rep* **21**, 2236-2250 (2017).
3. Rozo, M., Li, L. & Fan, C.M. Targeting beta1-integrin signaling enhances regeneration in aged and dystrophic muscle in mice. *Nat Med* **22**, 889-896 (2016).
4. Ralliere, C., Jagot, S., Sabin, N. & Gabillard, J.C. Dynamics of pax7 expression during development, muscle regeneration, and in vitro differentiation of satellite cells in rainbow trout (Oncorhynchus mykiss). *PLoS One* **19**, e0300850 (2024).
5. Wang, Y.X. & Rudnicki, M.A. Satellite cells, the engines of muscle repair. *Nat Rev Mol Cell Biol* **13**, 127-133 (2011).
6. Anderson, J.E. Key concepts in muscle regeneration: muscle "cellular ecology" integrates a gestalt of cellular cross-talk, motility, and activity to remodel structure and restore function. *Eur J Appl Physiol* **122**, 273-300 (2022).
7. Zhang, W., Liu, Y. & Zhang, H. Extracellular matrix: an important regulator of cell functions and skeletal muscle development. *Cell Biosci* **11**, 65 (2021).
8. Koike, H., Manabe, I. & Oishi, Y. Mechanisms of cooperative cell-cell interactions in skeletal muscle regeneration. *Inflamm Regen* **42**, 48 (2022).
9. Abou-Khalil, R. *et al.* Autocrine and paracrine angiopoietin 1/Tie-2 signaling promotes muscle satellite cell self-renewal. *Cell Stem Cell* **5**, 298-309 (2009).
10. Kedlian, V.R. *et al.* Human skeletal muscle aging atlas. *Nat Aging* **4**, 727-744 (2024).
11. Su, J. *et al.* A novel atlas of gene expression in human skeletal muscle reveals molecular changes associated with aging. *Skelet Muscle* **5**, 35 (2015).
12. Day, K., Shefer, G., Shearer, A. & Yablonka-Reuveni, Z. The depletion of skeletal muscle satellite cells with age is concomitant with reduced capacity of single progenitors to produce reserve progeny. *Dev Biol* **340**, 330-343 (2010).
13. Petermann-Rocha, F. *et al.* Global prevalence of sarcopenia and severe sarcopenia: a systematic review and meta-analysis. *J Cachexia Sarcopenia Muscle* **13**, 86-99 (2022).
14. Munoz-Canoves, P., Neves, J. & Sousa-Victor, P. Understanding muscle regenerative decline with aging: new approaches to bring back youthfulness to aged stem cells. *FEBS J* **287**, 406-416 (2020).
15. Rizk, J., Sahu, R. & Duteil, D. An overview on androgen-mediated actions in skeletal muscle and adipose tissue. *Steroids* **199**, 109306 (2023).
16. Conboy, I.M. & Rando, T.A. The regulation of Notch signaling controls satellite cell activation and cell fate determination in postnatal myogenesis. *Dev Cell* **3**, 397-409 (2002).
17. Seo, J.Y., Kim, J.H. & Kong, Y.Y. Unraveling the Paradoxical Action of Androgens on Muscle Stem Cells. *Mol Cells* **42**, 97-103 (2019).
18. Niel, L., Willemsen, K.R., Volante, S.N. & Monks, D.A. Sexual dimorphism and androgen regulation of satellite cell population in differentiating rat levator ani muscle. *Dev Neurobiol* **68**, 115-122 (2008).
19. Diel, P., Baadners, D., Schlupmann, K., Velders, M. & Schwarz, J.P. C2C12 myoblastoma cell differentiation and proliferation is stimulated by androgens and associated with a modulation of myostatin and Pax7 expression. *J Mol Endocrinol* **40**, 231-241 (2008).
20. Chen, Y., Zajac, J.D. & MacLean, H.E. Androgen regulation of satellite cell function. *J Endocrinol* **186**, 21-31 (2005).
21. Klose, A. *et al.* Castration induces satellite cell activation that contributes to skeletal muscle maintenance. *JCSM Rapid Commun* **1** (2018).
22. Sakai, H. & Imai, Y. Cell-specific functions of androgen receptor in skeletal muscles. *Endocr J* **71**, 437-445 (2024).

23. Sinha-Hikim, I., Taylor, W.E., Gonzalez-Cadavid, N.F., Zheng, W. & Bhasin, S. Androgen receptor in human skeletal muscle and cultured muscle satellite cells: up-regulation by androgen treatment. *J Clin Endocrinol Metab* **89**, 5245-5255 (2004).
24. Ghaibour, K. *et al.* Androgen receptor coordinates muscle metabolic and contractile functions. *J Cachexia Sarcopenia Muscle* **14**, 1707-1720 (2023).
25. Chambon, C. *et al.* Myocytic androgen receptor controls the strength but not the mass of limb muscles. *Proc Natl Acad Sci U S A* **107**, 14327-14332 (2010).
26. Oprescu, S.N., Yue, F., Qiu, J., Brito, L.F. & Kuang, S. Temporal Dynamics and Heterogeneity of Cell Populations during Skeletal Muscle Regeneration. *iScience* **23**, 100993 (2020).
27. McKellar, D.W. *et al.* Large-scale integration of single-cell transcriptomic data captures transitional progenitor states in mouse skeletal muscle regeneration. *Commun Biol* **4**, 1280 (2021).
28. Yue, F. *et al.* Lipid droplet dynamics regulate adult muscle stem cell fate. *Cell Rep* **38**, 110267 (2022).
29. Morroni, J. *et al.* Injury-experienced satellite cells retain long-term enhanced regenerative capacity. *Stem Cell Res Ther* **14**, 246 (2023).
30. Brun, C.E. *et al.* GLI3 regulates muscle stem cell entry into G(Alert) and self-renewal. *Nat Commun* **13**, 3961 (2022).
31. Barsky, S.T. & Monks, D.A. The role of androgens and global and tissue-specific androgen receptor expression on body composition, exercise adaptation, and performance. *Biol Sex Differ* **16**, 28 (2025).
32. Chinvattanachot, G., Rivas, D. & Duque, G. Mechanisms of muscle cells alterations and regeneration decline during aging. *Ageing Res Rev* **102**, 102589 (2024).
33. Serra, C. *et al.* Testosterone improves the regeneration of old and young mouse skeletal muscle. *J Gerontol A Biol Sci Med Sci* **68**, 17-26 (2013).
34. Oura, M. *et al.* Testosterone/androgen receptor antagonizes immobility-induced muscle atrophy through Inhibition of myostatin transcription and inflammation in mice. *Sci Rep* **15**, 10568 (2025).
35. Lai, Y. *et al.* Multimodal cell atlas of the ageing human skeletal muscle. *Nature* **629**, 154-164 (2024).
36. Dubois, V., Laurent, M., Boonen, S., Vanderschueren, D. & Claessens, F. Androgens and skeletal muscle: cellular and molecular action mechanisms underlying the anabolic actions. *Cell Mol Life Sci* **69**, 1651-1667 (2012).
37. Sheppard, R.L., Spangenburg, E.E., Chin, E.R. & Roth, S.M. Androgen receptor polyglutamine repeat length affects receptor activity and C2C12 cell development. *Physiol Genomics* **43**, 1135-1143 (2011).
38. Fu, S., Lin, X., Yin, L. & Wang, X. Androgen receptor regulates the proliferation of myoblasts under appropriate or excessive stretch through IGF-1 receptor mediated p38 and ERK1/2 pathways. *Nutr Metab (Lond)* **18**, 85 (2021).
39. Fu, S., Hu, J., Wang, G., Qian, Z. & Wang, X. Androgen receptor regulates the differentiation of myoblasts under cyclic mechanical stretch and its upstream and downstream signals. *Int J Biol Macromol* **281**, 136257 (2024).
40. Dubois, V. *et al.* Androgen Deficiency Exacerbates High-Fat Diet-Induced Metabolic Alterations in Male Mice. *Endocrinology* **157**, 648-665 (2016).
41. Rocchi, A. *et al.* Glycolytic-to-oxidative fiber-type switch and mTOR signaling activation are early-onset features of SBMA muscle modified by high-fat diet. *Acta Neuropathol* **132**, 127-144 (2016).
42. Campbell, M.D., Djukovic, D., Raftery, D. & Marcinek, D.J. Age-related changes of skeletal muscle metabolic response to contraction are also sex-dependent. *J Physiol* **603**, 69-86 (2025).
43. Grevendonk, L. *et al.* Impact of aging and exercise on skeletal muscle mitochondrial capacity, energy metabolism, and physical function. *Nat Commun* **12**, 4773 (2021).

44. Kobayashi, A., Azuma, K., Ikeda, K. & Inoue, S. Mechanisms Underlying the Regulation of Mitochondrial Respiratory Chain Complexes by Nuclear Steroid Receptors. *Int J Mol Sci* **21** (2020).
45. Jomova, K. *et al.* Reactive oxygen species, toxicity, oxidative stress, and antioxidants: chronic diseases and aging. *Arch Toxicol* **97**, 2499-2574 (2023).
46. Lee, J. *et al.* Androgen Deprivation Therapy-Induced Muscle Loss and Fat Gain Predict Cardiovascular Events in Prostate Cancer Patients. *J Cachexia Sarcopenia Muscle* **16**, e13844 (2025).
47. Argiles, J.M., Campos, N., Lopez-Pedrosa, J.M., Rueda, R. & Rodriguez-Manas, L. Skeletal Muscle Regulates Metabolism via Interorgan Crosstalk: Roles in Health and Disease. *J Am Med Dir Assoc* **17**, 789-796 (2016).
48. Penvose, A., Keenan, J.L., Bray, D., Ramlall, V. & Siggers, T. Comprehensive study of nuclear receptor DNA binding provides a revised framework for understanding receptor specificity. *Nat Commun* **10**, 2514 (2019).
49. Gelman, L. *et al.* Integrating nuclear receptor mobility in models of gene regulation. *Nucl Recept Signal* **4**, e010 (2006).
50. Hager, G.L., Nagaich, A.K., Johnson, T.A., Walker, D.A. & John, S. Dynamics of nuclear receptor movement and transcription. *Biochim Biophys Acta* **1677**, 46-51 (2004).
51. Stavreva, D.A. *et al.* Nuclear Receptors Dynamics and Gene Regulation in Response to Ultradian Hormone Pulses. *Endocrinology* **166**, bqaf043.034 (2025).
52. Forouhan, M. *et al.* AR cooperates with SMAD4 to maintain skeletal muscle homeostasis. *Acta Neuropathol* **143**, 713-731 (2022).
53. Nath, S.R. *et al.* Androgen receptor polyglutamine expansion drives age-dependent quality control defects and muscle dysfunction. *J Clin Invest* **128**, 3630-3641 (2018).
54. Arnold, F.J., Pluciennik, A. & Merry, D.E. Impaired Nuclear Export of Polyglutamine-Expanded Androgen Receptor in Spinal and Bulbar Muscular Atrophy. *Sci Rep* **9**, 119 (2019).
55. Shiina, H. *et al.* Premature ovarian failure in androgen receptor-deficient mice. *Proc Natl Acad Sci U S A* **103**, 224-229 (2006).
56. Murphy, M.M., Lawson, J.A., Mathew, S.J., Hutcheson, D.A. & Kardon, G. Satellite cells, connective tissue fibroblasts and their interactions are crucial for muscle regeneration. *Development* **138**, 3625-3637 (2011).
57. Tosic, M. *et al.* Lsd1 regulates skeletal muscle regeneration and directs the fate of satellite cells. *Nat Commun* **9**, 366 (2018).
58. Chenu, C. *et al.* Testosterone Prevents Cutaneous Ischemia and Necrosis in Males Through Complementary Estrogenic and Androgenic Actions. *Arterioscler Thromb Vasc Biol* **37**, 909-919 (2017).
59. Rovito, D. *et al.* Myod1 and GR coordinate myofiber-specific transcriptional enhancers. *Nucleic Acids Res* **49**, 4472-4492 (2021).
60. Simon, A. *et al.* Transcriptomic characterization of postnatal muscle maturation. *Dis Model Mech* **18** (2025).
61. Cigrang, M. *et al.* Pan-inhibition of super-enhancer-driven oncogenic transcription by next-generation synthetic ecteinascidins yields potent anti-cancer activity. *Nat Commun* **16**, 512 (2025).
62. Ghaibour, K. *et al.* An Efficient Protocol for CUT&RUN Analysis of FACS-Isolated Mouse Satellite Cells. *J Vis Exp* (2023).
63. Janssens, D.H. *et al.* Automated in situ chromatin profiling efficiently resolves cell types and gene regulatory programs. *Epigenetics Chromatin* **11**, 74 (2018).
64. Langmead, B. & Salzberg, S.L. Fast gapped-read alignment with Bowtie 2. *Nat Methods* **9**, 357-359 (2012).
65. Ramirez, F., Dundar, F., Diehl, S., Gruning, B.A. & Manke, T. deepTools: a flexible platform for exploring deep-sequencing data. *Nucleic Acids Res* **42**, W187-191 (2014).

66. Quinlan, A.R. & Hall, I.M. BEDTools: a flexible suite of utilities for comparing genomic features. *Bioinformatics* **26**, 841-842 (2010).
67. Meers, M.P., Tenenbaum, D. & Henikoff, S. Peak calling by Sparse Enrichment Analysis for CUT&RUN chromatin profiling. *Epigenetics Chromatin* **12**, 42 (2019).
68. Zhang, Y. *et al.* Model-based analysis of ChIP-Seq (MACS). *Genome Biol* **9**, R137 (2008).
69. Ye, T. *et al.* seqMINER: an integrated ChIP-seq data interpretation platform. *Nucleic Acids Res* **39**, e35 (2011).
70. Cai, Q. *et al.* LSD1 inhibition circumvents glucocorticoid-induced muscle wasting of male mice. *Nat Commun* **15**, 3563 (2024).
71. Livak, K.J. & Schmittgen, T.D. Analysis of relative gene expression data using real-time quantitative PCR and the 2(-Delta Delta C(T)) Method. *Methods* **25**, 402-408 (2001).
72. Dobin, A. *et al.* STAR: ultrafast universal RNA-seq aligner. *Bioinformatics* **29**, 15-21 (2013).
73. Anders, S., Pyl, P.T. & Huber, W. HTSeq--a Python framework to work with high-throughput sequencing data. *Bioinformatics* **31**, 166-169 (2015).
74. Love, M.I., Huber, W. & Anders, S. Moderated estimation of fold change and dispersion for RNA-seq data with DESeq2. *Genome Biol* **15**, 550 (2014).
75. Szklarczyk, D. *et al.* The STRING database in 2023: protein-protein association networks and functional enrichment analyses for any sequenced genome of interest. *Nucleic Acids Res* **51**, D638-D646 (2023).
76. Wang, J., Duncan, D., Shi, Z. & Zhang, B. WEB-based GEne SeT AnaLysis Toolkit (WebGestalt): update 2013. *Nucleic Acids Res* **41**, W77-83 (2013).
77. de Hoon, M.J., Imoto, S., Nolan, J. & Miyano, S. Open source clustering software. *Bioinformatics* **20**, 1453-1454 (2004).
78. Lu, Y., Lu, S., Fotouhi, F., Deng, Y. & Brown, S.J. Incremental genetic K-means algorithm and its application in gene expression data analysis. *BMC Bioinformatics* **5**, 172 (2004).
79. Raine, A., Liljedahl, U. & Nordlund, J. Data quality of whole genome bisulfite sequencing on Illumina platforms. *PLoS One* **13**, e0195972 (2018).
80. Lun, A.T.L. *et al.* EmptyDrops: distinguishing cells from empty droplets in droplet-based single-cell RNA sequencing data. *Genome Biol* **20**, 63 (2019).
81. Satija, R., Farrell, J.A., Gennert, D., Schier, A.F. & Regev, A. Spatial reconstruction of single-cell gene expression data. *Nat Biotechnol* **33**, 495-502 (2015).
82. Jin, S. *et al.* Inference and analysis of cell-cell communication using CellChat. *Nat Commun* **12**, 1088 (2021).
83. Riba, A. *et al.* Cell cycle gene regulation dynamics revealed by RNA velocity and deep-learning. *Nat Commun* **13**, 2865 (2022).
84. Schneider, C.A., Rasband, W.S. & Eliceiri, K.W. NIH Image to ImageJ: 25 years of image analysis. *Nat Methods* **9**, 671-675 (2012).

ACKNOWLEDGMENTS

We thank Dr. J. Laporte (IGBMC) for generously providing the LHCN-M2 and C79 cell lines. We are grateful to Anastasia Bannwarth, Nikola Djordjevic, and Régis Lutzing for their valuable technical support, and Valentine Gilbart, Tao Ye and Céline Keime for excellent bioinformatics assistance. We extend our gratitude to Graciela Ruiz for her valuable scientific expertise. We are grateful to Prof. S. Kato for providing the AR floxed mice, and Prof. G. Kardon for the *Pax7*-CreER^{T2} line. We acknowledge the support of the IGBMC core facilities, including the animal facility, microscopy and electron microscopy platforms, biochemistry, cell culture service, flow cytometry, and histopathology services, as well as the Mouse Clinical Institute (ICS, Illkirch-Graffenstaden, France) and GenomEast facility, a member of the 'France Génomique' consortium (ANR-10-INBS-0009).

This work was supported by the Interdisciplinary Thematic Institute IMCBio as part of the ITI 2021-2028 program of the University of Strasbourg, the Centre National pour la Recherche Scientifique (CNRS), Institut national de la santé et de la recherche médicale (Inserm), from IdEx Unistra (ANR-10-IDEX-0002), SFRI-STRAT'US (ANR 20-SFRI-0012) and EUR IMCBio (ANR-17-EURE-0023) projects, under the framework of the French Investments for the Future Programme. Additional support was provided by Inserm, CNRS, Unistra, IGBMC, AFM-Téléthon (grant application #24376), and the Agence Nationale de la Recherche (ANR-10-BLAN-1108, ANR-24-CE14-0247-01). J.G.R. received funding from the Programme CDFA-07-22 from the Université franco-allemande and Ministère de l'Enseignement Supérieur de la Recherche et de l'Innovation. K.C.G. received funding by the Association pour la Recherche à l'IGBMC (ARI), E.C by MESRI, Q.C by ANR (ANDROMETAMUS, ANR-24-CE14-0247-01), and R.S. by IMCBio. Anastasia Bannwarth received funding from AFM-Téléthon (grant application #24376) for technical assistance.

AUTHOR CONTRIBUTIONS

D.D., J.G.R., and K.C.G. formulated the initial hypothesis. J.G.R., K.C.G., S.S.C., A.B., Q.C., G. R., E.C., and R.S. carried out functional, molecular, and histological experiments. D.D., J.G.R., N.M., and G.Z. executed bioinformatics analyses. N.M., H.J., and E.G. took responsibility of imaging analyses. A.F. conducted *in situ* myofiber contraction experiments. J-F.A. and C.F. provided DHT pellets and performed initial *in vivo* tests. J.G.R., K.C.G., D.M., and D.D. took primary responsibility for data analysis and writing the manuscript.

Declaration of interests

The authors declare no competing interests.

ETHICS DECLARATIONS

Competing interests

The authors declare no competing interests.

FIGURE LEGENDS

Figure 1: Absence of MuSC-AR impairs muscle regenerative capacities at puberty.

(A) Representative hematoxylin and eosin (H&E) staining of tibialis anterior (TA) muscles of 3-month-old control and $AR^{(i)sat-/Y}$ male mice under non-injured (NI) condition, and at 7 days post-injury (7 dpi). Black arrows indicate centrally nucleated fibers. Blue arrows point to immune infiltration. Yellow arrows denote necrotic fibers. Green arrows show interstitial space. Pink arrows label misshaped regenerating myofibers. Orange arrows mark fibrosis. Scale bars, 75 µm.

(B) Ultrastructure analysis of NI and 7-days-injured TA of 3-month-old control and $AR^{(i)sat-/Y}$ male mice. Z: Z-line, M: M-line, I: I-bands, A: A-band. Black arrows indicate M-line disturbances. Red arrows point to Z-line disruption. Pink arrows depict T-tubules misalignments. Orange arrows denote fibrosis. Green arrows show the A-band placement. Yellow arrows label the I-bands placements. Scale bars, 1 µm.

(C) Distribution of myofibers cross-section area (CSA) in TA muscles of control and $AR^{(i)sat-/Y}$ male mice 7 dpi. Data are presented as mean ± SEM. Statistical test used Two-way ANOVA with Sidak's correction.

(D) *In situ* single-fiber isometric force of 28-days-injured TA of control and $AR^{(i)sat-/Y}$ male mice. Data are presented as mean ± SEM. Statistical test used was two-tailed Mann-Whitney test; $*p < 0.05$.

(E-F) Representative immunofluorescent labeling of PAX7 (in red) **(E)**, and corresponding quantification of the number of PAX7-positive cells **(F)** in 7-days-injured TA of control and $AR^{(i)sat-/Y}$ male mice. White arrows point to PAX7-positive cells. Nuclei were stained with DAPI. Data are presented as mean ± SEM. Statistical test used is two-tailed Mann-Whitney test; ns, non-significant; $** = p < 0.01$; $*** = p < 0.001$.

(G-H) Heatmap depicting the mean centered normalized expression of indicated genes selected from bulk RNA-sequencing analysis performed in 7-days-injured TA of 3-month-old control and $AR^{(i)sat-/Y}$ male mice **(G)**, and corresponding pathway analysis **(H)**.

(I) Violin plots representing the normalized read counts of the indicated genes, selected from bulk RNA-sequencing analysis performed in 7-days-injured TA of control and $AR^{(i)sat-/Y}$ male mice. Statistical test used is Wald test; $** = p < 0.01$; $*** = p < 0.001$.

(J) Representative immunofluorescent detection of DMD (in red), in 7-days-injured TA of control and $AR^{(i)sat-/Y}$ male mice. Nuclei were stained with DAPI. White arrows depict fibers emerging within other fibers. Scale bars, 100 µm.

(K) Representative immunofluorescent detection of DMD (in red), and sarcomeric alpha actinin (ACTN1) (in green), in 7-days-injured transversal and longitudinal sections of TA of control and $AR^{(i)sat-/Y}$ male mice. Nuclei were stained with DAPI. White arrows point to nuclei. Yellow arrows denote sarcolemma discontinuation. Red arrows show ACTN1 aggregates. Pink arrows denote stairs-shape in regenerating fibers. Scale bars, 50 µm.

(L-M) Representative immunofluorescent detection of embryonic myosin (MYH3) (in green), and LAMA2 (in magenta) **(L)**, and corresponding quantification of the number of MYH3-positive cells **(M)** in 5- and 7-days-injured TA of control and $AR^{(i)sat-/Y}$ male mice. Nuclei were stained with DAPI. Scale bars, 85 µm. Data are presented as mean ± SEM. Statistical test used is Two-way ANOVA with Tukey correction; ns, non-significant; ** = $p < 0.01$; *** = $p < 0.001$; ns = non-significant.

(N-O) Violin plots representing the normalized read counts of the indicated genes encoding myosin heavy chain (*Myh*s) isoforms **(N)**, or subunits of the electron transport chain complexes **(O)** selected from bulk RNA-sequencing analysis performed in 7-days-injured TA of control and $AR^{(i)sat-/Y}$ male mice. Statistical test used is Wald test; * = $p < 0.05$; ** = $p < 0.01$; *** = $p < 0.001$.

(P) Representative histochemical staining of NADH dehydrogenase (NADH-DH) and COX activities in 7-days-injured TA of 3-month-old control and $AR^{(i)sat-/Y}$ male mice. Oxidative and intermediate fibers are darkly and moderately stained, respectively; glycolytic fibers are lightly stained. Scale bars, 200 µm.

(Q) Mitochondrial respiration profile of vehicle and 100 nM flutamide-treated LHCN-M2 cells, assessed using the Seahorse Mito Stress Test, following sequential injection of oligomycin, carbonyl cyanide-p-trifluoromethoxyphenylhydrazone (FCCP), and rotenone/AA, and expressed as oxygen consumption rate (OCR). Data are normalized to total nuclear counts, and presented as mean ± SEM. Statistical test used was two-tailed Mann-Whitney test; * = $p < 0.05$.

Figure 2: Characterization of AR cistrome and transcriptome in MuSC at puberty.

(A) Heatmap depicting the mean centered normalized expression of indicated genes selected from bulk RNA-sequencing analysis performed in 7-days-injured TA of 3-month-old control and $AR^{(i)sat-/Y}$ male mice.

(B) Pathway analysis of down- and up-regulated genes in 7-days-injured TA of control and $AR^{(i)sat-/Y}$ male mice.

(C) Violin plots representing the normalized read counts of the indicated genes, selected from bulk RNA-sequencing analysis performed in 7-days-injured TA of control and $AR^{(i)sat-/Y}$ male mice. Statistical test used is Wald test; ** = $p < 0.01$; *** = $p < 0.001$.

(D) HOMER known and *de novo* motif analyses of AR-bound DNA sequences from 7-day-injured TA of male mice.

(E) Pathway analysis performed on AR target genes identified by CUT&RUN in MuSC of 7-day-injured TA of male mice. Pathways of interest are squared in red.

(F) Cumulative number of down-regulated genes **(C)**, and up-regulated genes **(D)** in MuSC of 7-day-injured TA of male mice, with an AR peak located at the indicated distances from their TSS.

(G) AR localization at the *Ar*, *Fzd4*, *Kdmc4*, *Myh1*, *Tead1*, and *Mylk4* loci, with binding sites shown in red.

Figure 3: MuSC microenvironment is altered in the absence of AR.

(A-B) Uniform manifold approximation and projection (UMAP) visualization of single cells **(A)**, and respective percentage of cell types **(B)**, from 5-days-injured control and $AR^{(i)sat-/Y}$ TA of 3-month-old mice, colored by cluster identity.

(C-D) Percentage of macrophages **(C)**, immune cells, FAPs and MuSC **(D)**, in 5-days-injured TA of control and $AR^{(i)sat-/Y}$ mice, analyzed from flow-cytometry data conducted at the indicated time-point. Data are presented as mean ± SEM. Statistical test used was two-tailed Mann-Whitney test; ns, non-significant; * = $p < 0.05$, *** = $p < 0.001$.

(E) Violin plot of *Ar* transcript levels in the indicated cell populations identified from 5-days-injured TA of control and $AR^{(i)sat-/Y}$ mice.

(F) Schematic diagram of cell-cell communication between MuSC and other TA constitutive cells types in 5-days-injured TA of control and $AR^{(i)sat-/Y}$ mice.

(G-H) Violin plots representing the transcript levels of macrophage type-1 **(G)**, and macrophage type-2 markers **(H)**, selected from scRNA-seq analysis performed in 5-days-injured TA of control and $AR^{(i)sat-/Y}$ mice.

(I) Percentage of immune cells, FAPs and MuSC, in 7-days-injured TA of 3-month-old control and $AR^{(i)sat-/Y}$ mice, analyzed from flow-cytometry data conducted at the indicated time-point. Data are presented as mean ± SEM. Statistical test used was two-tailed Mann-Whitney test; ns, non-significant; ** = $p < 0.01$; *** = $p < 0.001$.

(J) Representative immunofluorescent detection of F4/80 (in green), in 7-days-injured TA of control and $AR^{(i)sat-/Y}$ mice. White arrows depict inter-fiber macrophages. Red arrows point to intra-fibers macrophages. Nuclei were stained with DAPI. Scale bars, 100 µm for the main, 30 µm for magnified inset.

(K) Representative Sirius Red histochemical staining visualized under brightfield (upper panel), and polarized light (lower panel), in 7-days-injured TA of control and $AR^{(i)sat-/Y}$ mice. Black arrows point to collagen fibers deposition. White arrows depict type I collagen fibers. Cyan blue arrows indicate type III collagen fibers. Scale bars, 250 µm for the main, 90 µm for magnified inset.

(L-M) Quantification of Sirius Red area from brightfield analysis **(L)**, and fibrosis composition **(M)** of 7-days-injured TA of control and $AR^{(i)sat-/Y}$ mice. Data are presented as mean ± SEM. Statistical test used was two-tailed Mann-Whitney test; ns, non-significant; ** = $p < 0.01$.

(N) Representative immunofluorescent detection of perilipin (PLIN1) (red) in 5- and 7-days-injured TA of control and $AR^{(i)sat-/Y}$ mice. White arrows point to adipocytes. Nuclei were stained with DAPI. Scale bars, 100 µm.

(O) Schematic overview of MuSC-AR influence in the regenerative niche at puberty. AR signaling in MuSC promotes type 1 (M1) macrophage polarization while limiting the transition to type 2 (M2) macrophages. Additionally, it restrains FAPs from excessive extracellular matrix production, and adipogenic differentiation. Green arrows indicate activation, red arrows indicate inhibition, and black arrows represent undefined interactions.

Figure 4: AR deficiency in MuSC favors symmetric differentiation over asymmetric division or symmetric self-renewal

(A) UMAP visualization of MuSC reclusters from 5-days-injured control and $AR^{(i)sat-/Y}$ TA of 3-month-old mice, colored by cluster identity.

(B) Violin plots representing the expression level of indicated genes in MuSC reclusters, selected from scRNA-seq analysis performed in 5-days-injured TA of control and $AR^{(i)sat-/Y}$ mice.

(C) Cell cycle distribution across MuSC reclusters in 5-days-injured TA of control and $AR^{(i)sat-/Y}$ mice, showing the proportion of cells in G1, S, and G2/M phases.

(D-F) Representative immunofluorescent detection of PAX7 (magenta), and KI67 (green) **(D)**, and corresponding quantifications in 5- **(E)** and 7-days **(F)** injured TA of control and $AR^{(i)sat-/Y}$ mice. Nuclei were stained with DAPI. Scale bars, 100 µm for the main, 30 µm for magnified inset. Statistical test used is Two-way ANOVA with Tukey correction; ns, non-significant; * = $p < 0.05$; *** = $p < 0.001$.

(G-I) Representative immunofluorescent detection of PAX7 (magenta) and MYOG (green), and corresponding quantifications in 5- **(H)** and 7-days **(I)** injured TA of control and $AR^{(i)sat-/Y}$ mice. Nuclei were stained with DAPI. Scale bars, 100 µm for the main, 30 µm for magnified inset. Data are presented as mean ± SEM. Statistical test used is Two-way ANOVA with Tukey correction; ns, non-significant; * = $p < 0.05$; *** = $p < 0.001$.

(J) Representative HE staining of TA muscles of control and $AR^{(i)sat-/Y}$ mice, 7 (single injury) and 28+7 (double injury) days after injury. Cyan blue arrows denote inflammatory cells. Green arrows point to interstitial space. Black arrows depict central nuclei. Pink arrows show misshaped fibers. Scale bars, 100 µm.

(K) Representative immunofluorescent detection of DMD (red), and PAX7 (green), of 28+7-days-injured control and $AR^{(i)sat-/Y}$ mouse TA. Scale bars, 50 µm.

(L) Quantification of the number of PAX7-positive cells in 28+7-days-injured control and $AR^{(i)sat-/Y}$ mouse TA. Data are presented as mean ± SEM. Statistical test used was two-tailed Mann-Whitney test; * = $p < 0.05$.

(M) Schematic overview of MuSC-autonomous regulation by AR signaling at puberty. AR activity in MuSC promotes symmetric divisions that replenish the stem cell pool. Conversely, it inhibits asymmetric divisions, precisely symmetric differentiation, where both daughter cells adopt a myoblast fate. Green arrows indicate activation, and red arrows indicate inhibition.

Figure 5: MuSC-AR exhibits time-dependent binding to target genes following injury

(A) HOMER known and *de novo* motif analyses of AR-bound DNA sequences from 5-day-injured TA of male mice.

(B) Pathway analysis performed on AR common target genes identified in MuSC of 5-day-injured TA of male mice.

(C-D) Cumulative number of down-regulated genes **(C)**, and up-regulated genes **(D)** in MuSC of 5-day-injured TA of male mice, with an AR peak located at the indicated distances from their TSS.

(E) AR localization at the *Clock*, *Eif2d*, and *Psma4* loci. Binding sites are indicated in red.

(F) Average tag density profiles, and corresponding tag density map of AR in NI, 5- and 7-days injured TA muscles of male mice, +/− 2 kb from the AR peak center.

(G) Overlap among genes bound by AR, in NI, 5- and 7-days injured TA muscles of male mice.

(H) AR localization in MuSC in NI, 5- and 7-days injured TA muscles of male mice, at indicated loci.

(I) Schematic overview of AR-mediated temporal regulation and chromatin binding dynamics in MuSC during regeneration at puberty. AR displays stage-specific chromatin occupancy throughout muscle regeneration. In uninjured muscle, MuSC-AR supports homeostasis. Following injury, AR translocates to genomic regions that drive regenerative programs, favoring genes involved in MuSC activation and proliferation at 5 dpi, and shifting toward loci promoting differentiation and maturation by 7 dpi.

Figure 6: Age-related androgen decline alters skeletal muscle repair machinery

(A) Serum testosterone levels of control male mice at indicated time-points. Basal level is represented by a dashed line. Data are presented as mean ± SEM. Statistical test used is Ordinary One-way ANOVA relative to 2-month-old mice. ns, non-significant; * = $p < 0.05$; ** = $p < 0.01$.

(B) Relative *Ar* transcript levels in TA muscles of control mice at indicated time-points. Data are presented as mean ± SEM. Statistical test used is Ordinary One-way ANOVA. *** = $p < 0.001$.

(C-D) Representative western blot analysis **(C)**, and corresponding quantification of the indicated proteins **(D)** in TA of 3-month-old (young) and 21-month-old (old) control male mice. GAPDH was used

as a loading control. Data are presented as mean ± SEM. Statistical test used was two-tailed Mann-Whitney test; *** = $p < 0.001$.

(E) Relative *Pax7* transcript levels in TA muscles from young and old control male mice. Data are presented as mean ± SEM. Statistical test used was two-tailed Mann-Whitney test; * = $p < 0.05$.

(F) Representative hematoxylin and eosin (H&E) staining of TA muscles of control and $AR^{(i)sat-/Y}$ old male mice under non-injured (NI) condition, and at 7 dpi. Black arrows indicate centrally nucleated fibers. Blue arrows point to immune infiltration. Yellow arrows denote necrotic fibers. Green arrows show interstitial space. Pink arrows label misshaped regenerating myofibers. Orange arrows mark fibrosis. Scale bars, 75 µm.

(G) Ultrastructure analysis of NI and 7-days-injured TA of control and $AR^{(i)sat-/Y}$ old male mice. Z: Z-line, M: M-line, I: I-bands, A: A-band. Black arrows indicate M-line disturbances. Red arrows point to Z-line disruption. Pink arrows depict T-tubules misalignments. Orange arrows denote fibrosis. Green arrows show the A-band placement. Yellow arrows label the I-bands placements. Scale bars, 1 µm.

(H-I) Representative immunofluorescent labeling of PAX7 (in red) **(H)**, and corresponding quantification of the number of PAX7-positive cells **(I)** in 7-days-injured TA of control and $AR^{(i)sat-/Y}$ young and old male mice. White arrows point to PAX7-positive cells. Nuclei were stained with DAPI. Data are presented as mean ± SEM. Statistical test used is two-tailed Mann-Whitney test; ns, non-significant; ** = $p < 0.01$; *** = $p < 0.001$.

(J) Representative immunofluorescent detection of DMD (in red), in 7-days-injured TA of control and $AR^{(i)sat-/Y}$ old male mice. Nuclei were stained with DAPI. White arrows depict fibers emerging within other fibers. Scale bars, 100 µm.

(K-L) Representative HE staining **(K)**, and corresponding quantification of the average number of central nuclei **(L)** of TA muscles of control old Sham-operated or DHT-supplemented old male mice, 7 dpi. Cyan blue arrows point to immune infiltration. Black arrows denote central nuclei. White arrows show central or parallel nuclei alignments. Scale bars, 150 µm for transverse, and 100 µm for longitudinal sections. Data are presented as mean ± SEM. Statistical test used was two-tailed Mann-Whitney test; * = $p < 0.05$.

(M) Representative histochemical staining of NADH dehydrogenase (NADH-DH) and COX activities in 7-days-injured TA of control and $AR^{(i)sat-/Y}$ old male mice. Oxidative and intermediate fibers are darkly and moderately stained, respectively; glycolytic fibers are lightly stained. Scale bars, 200 µm.

(N) Representative Sirius Red histochemical staining visualized under brightfield in 7-days-injured TA of control and $AR^{(i)sat-/Y}$ old mice. Black arrows point to collagen fibers deposition. White arrows depict type I collagen fibers. Cyan blue arrows indicate type III collagen fibers. Scale bars, 250 µm for the main, 90 µm for magnified inset.

(O) Quantification of Sirius Red area from brightfield analysis of 7-days-injured TA of control and $AR^{(i)sat-/Y}$ old mice. Data are presented as mean ± SEM. Statistical test used was two-tailed Mann-Whitney test; ns, non-significant; ** = p < 0.01.

(P) Representative immunofluorescent detection of perilipin (PLIN1) (red) in 5- and 7-days-injured TA of control and $AR^{(i)sat-/Y}$ old mice. White arrows point to adipocytes. Nuclei were stained with DAPI. Scale bars, 100 µm.

Figure 7: Androgen receptor governs MuSC function in aged muscle through mechanisms that differ from those operating in the young.

(A-B) Heatmap depicting the mean centered normalized expression of down- and upregulated genes from SMART-seq analysis performed on control MuSC FACS-isolated from 7-day-injured TA of old and young mice **(A)**, and corresponding gene ontology enrichment **(B)**.

(C) Violin plots representing the normalized read counts of the indicated genes, selected from SMART-seq analysis performed control MuSC FACS-isolated from 7-day-injured TA of old and young mice. Statistical test used is Wald test; * = p < 0.05; ** = p < 0.01; *** = p < 0.001.

(D) Venn diagrams showing intersected genes among differentially expressed genes in MuSC of control old mice and $AR^{(i)sat-/Y}$ young mice.

(E-F) Cumulative number of down-regulated genes **(E)**, and up-regulated genes **(F)** in MuSC of 7-day-injured TA of old male mice, with an AR peak located at the indicated distances from their TSS.

(G) Venn diagrams showing intersected genes with AR peaks among differentially expressed genes in MuSC of control old mice and $AR^{(i)sat-/Y}$ young mice.

(H) Relative *AR* transcript levels in control LHCN-M2 and C79 myoblasts. Data are presented as mean ± SEM. Statistical test used was two-tailed Mann-Whitney test; ** = p < 0.01.

(I-J) Representative western blot analysis **(I)**, and corresponding quantification of the indicated proteins **(J)** in control LHCN-M2 and C79 myoblasts. α-TUBULIN (TUB) was used as a loading control. Data are presented as mean ± SEM. Statistical test used was two-tailed Mann-Whitney test; * = p < 0.05.

(K) Representative immunofluorescent detection of PAX7 (in green) and AR (in red), in LHCN-M2 and C79 cells. Scale bars, 100 µm for the main, 10 µm for magnified inset.

(L) Quantification of the percentage of high- and low/non-proliferative control LHCN-M2 and C79 myoblasts as determined by CellTrace analysis. Data are presented as mean ± SEM. Statistical test used is Two-way ANOVA with Tukey correction; *** = p< 0.001.

(M) Representative brightfield images of control (CTR) and AR-siRNA transfected (siRNA-hAR) LHCN-M2 and C79 cells, 0, 3- and 5-days post-differentiation (dpd). Black arrows show fibroblast-like non-differentiated cells. Red arrows label spindle-like differentiated cells. Scale bars, 100 µm.

FIGURE 1

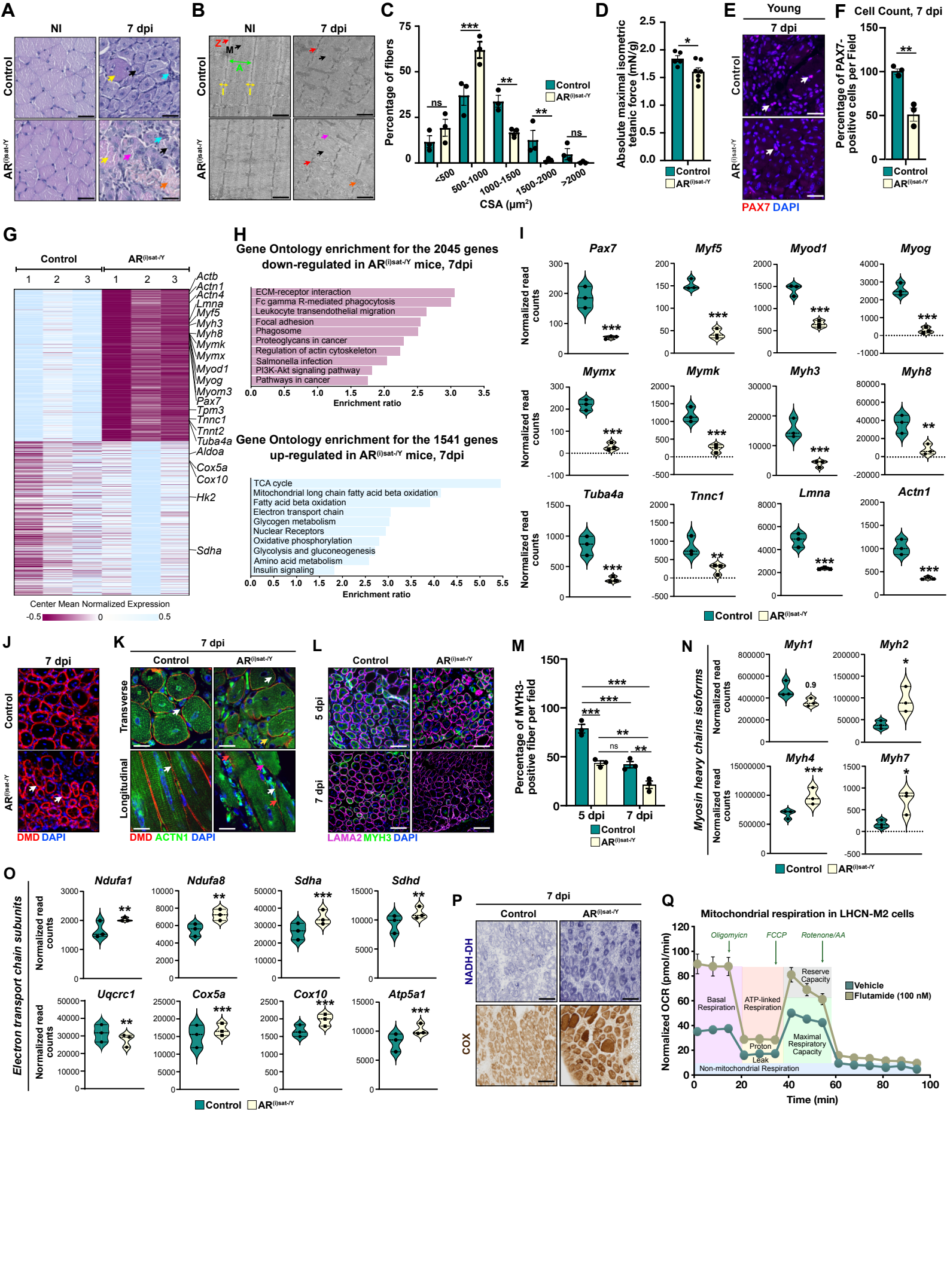
A
NI
7 dpi
Control
AR(i)sat-/Y
B
NI
7 dpi
Control
AR(i)sat-/Y
Z
M
A
I
C
Percentage of fibers
75
50
25
0
***
**
**
ns
ns
<500
500-1000
1000-1500
1500-2000
>2000
CSA (µm²)
Control
AR(i)sat-/Y
D
Absolute maximal isometric tetanic force (mN/g)
2.5
2.0
1.5
1.0
0.5
0.0
*
Control
AR(i)sat-/Y
E
Young
7 dpi
Control
AR(i)sat-/Y
PAX7 DAPI
F
Cell Count, 7 dpi
Percentage of PAX7-positive cells per Field
150
100
50
0
**
Control
AR(i)sat-/Y
G
Control
AR(i)sat-/Y
1
2
3
1
2
3
Actb
Actn1
Actn4
Lmna
Myf5
Myh3
Myh8
Mymk
Mymx
Myod1
Myog
Myom3
Pax7
Tpm3
Tnnc1
Tnnt2
Tuba4a
Aldoa
Cox5a
Cox10
Hk2
Sdha
Center Mean Normalized Expression
-0.5
0
0.5
H
Gene Ontology enrichment for the 2045 genes down-regulated in AR(i)sat-/Y mice, 7dpi
ECM-receptor interaction
Fc gamma R-mediated phagocytosis
Leukocyte transendothelial migration
Focal adhesion
Phagosome
Proteoglycans in cancer
Regulation of actin cytoskeleton
Salmonella infection
PI3K-Akt signaling pathway
Pathways in cancer
0.0
0.5
1.0
1.5
2.0
2.5
3.0
3.5
Enrichment ratio
Gene Ontology enrichment for the 1541 genes up-regulated in AR(i)sat-/Y mice, 7dpi
TCA cycle
Mitochondrial long chain fatty acid beta oxidation
Fatty acid beta oxidation
Electron transport chain
Glycogen metabolism
Nuclear Receptors
Oxidative phosphorylation
Glycolysis and gluconeogenesis
Amino acid metabolism
Insulin signaling
0.0
0.5
1.0
1.5
2.0
2.5
3.0
3.5
4.0
4.5
5.0
5.5
Enrichment ratio
I
Pax7
Myf5
Myod1
Myog
Mymx
Mymk
Myh3
Myh8
Tuba4a
Tnnc1
Lmna
Actn1
Normalized read counts
***
Control
AR(i)sat-/Y
J
7 dpi
Control
AR(i)sat-/Y
DMD DAPI
K
7 dpi
Control
AR(i)sat-/Y
Transverse
Longitudinal
DMD ACTN1 DAPI
L
Control
AR(i)sat-/Y
5 dpi
7 dpi
LAMA2 MYH3 DAPI
M
Percentage of MYH3-positive fiber per field
150
100
50
0
***
***
***
**
ns
**
5 dpi
7 dpi
Control
AR(i)sat-/Y
N
Myosin heavy chains isoforms
Normalized read counts
Myh1
Myh2
Myh4
Myh7
0.9
*
***
*
Control
AR(i)sat-/Y
O
Electron transport chain subunits
Normalized read counts
Ndufa1
Ndufa8
Sdha
Sdhd
Uqcrc1
Cox5a
Cox10
Atp5a1
**
***
Control
AR(i)sat-/Y
P
7 dpi
Control
AR(i)sat-/Y
NADH-DH
COX
Q
Mitochondrial respiration in LHCN-M2 cells
Oligomycin
FCCP
Rotenone/AA
Normalized OCR (pmol/min)
120
100
80
60
40
20
0
Basal Respiration
ATP-linked Respiration
Proton Leak
Reserve Capacity
Maximal Respiratory Capacity
Non-mitochondrial Respiration
Vehicle
Flutamide (100 nM)
0
20
40
60
80
100
Time (min)

FIGURE 2

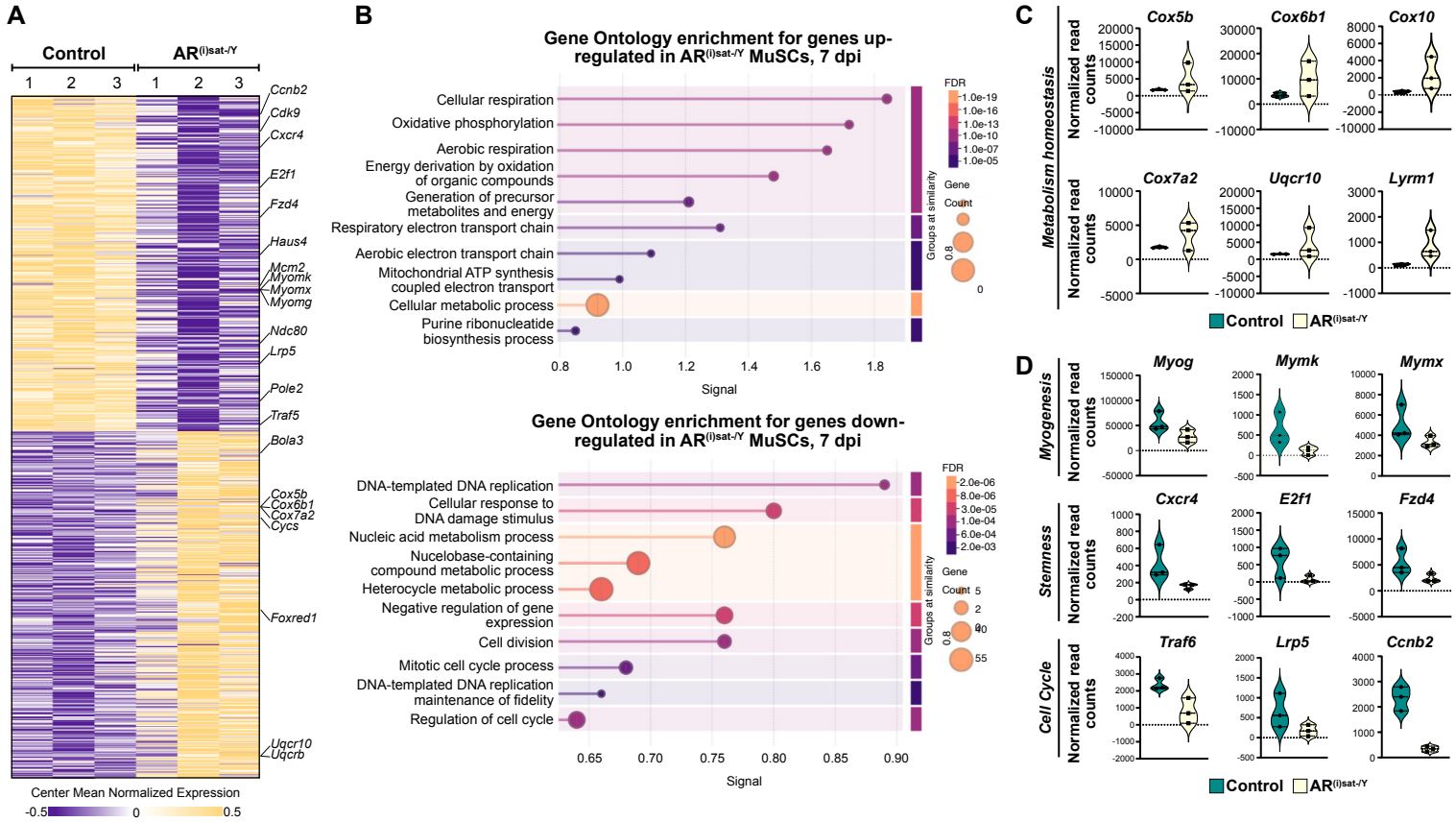

D

AR Known Motif Search

Name	Logo	p-value	% of Targets
ARE		1e-124	49.45 %
AR-half site		1e-17	68.13%

AR *de novo* Motif Search

Name	Logo	p-value	% of Targets
AR		1e-348	47.15 %
AR-half site		1e-13	8.79%

E

Pathway analysis on AR target genes in MuSCs, 7 dpi

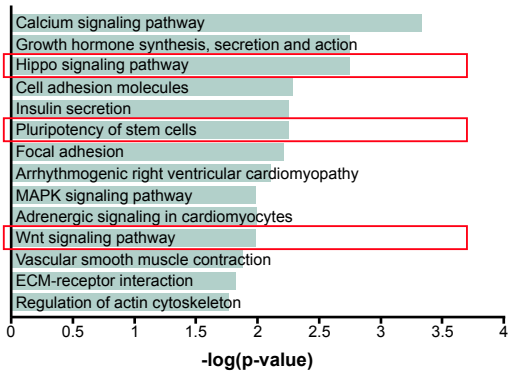

F

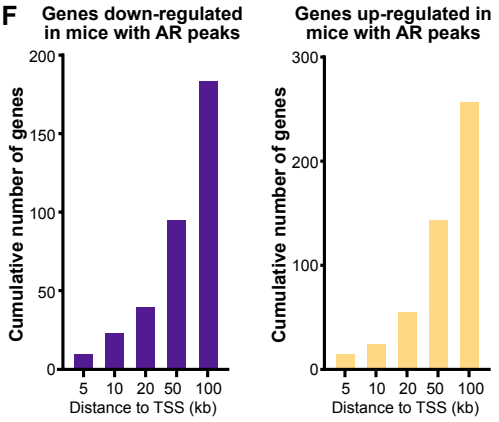

G

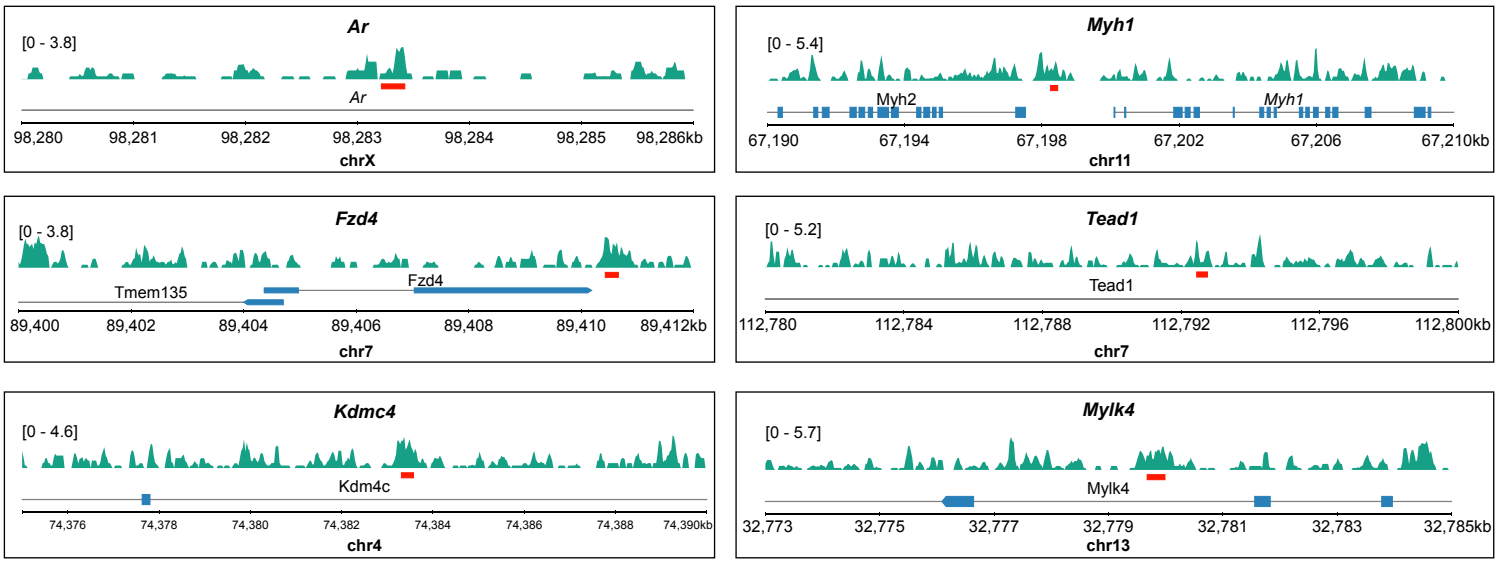

FIGURE 3

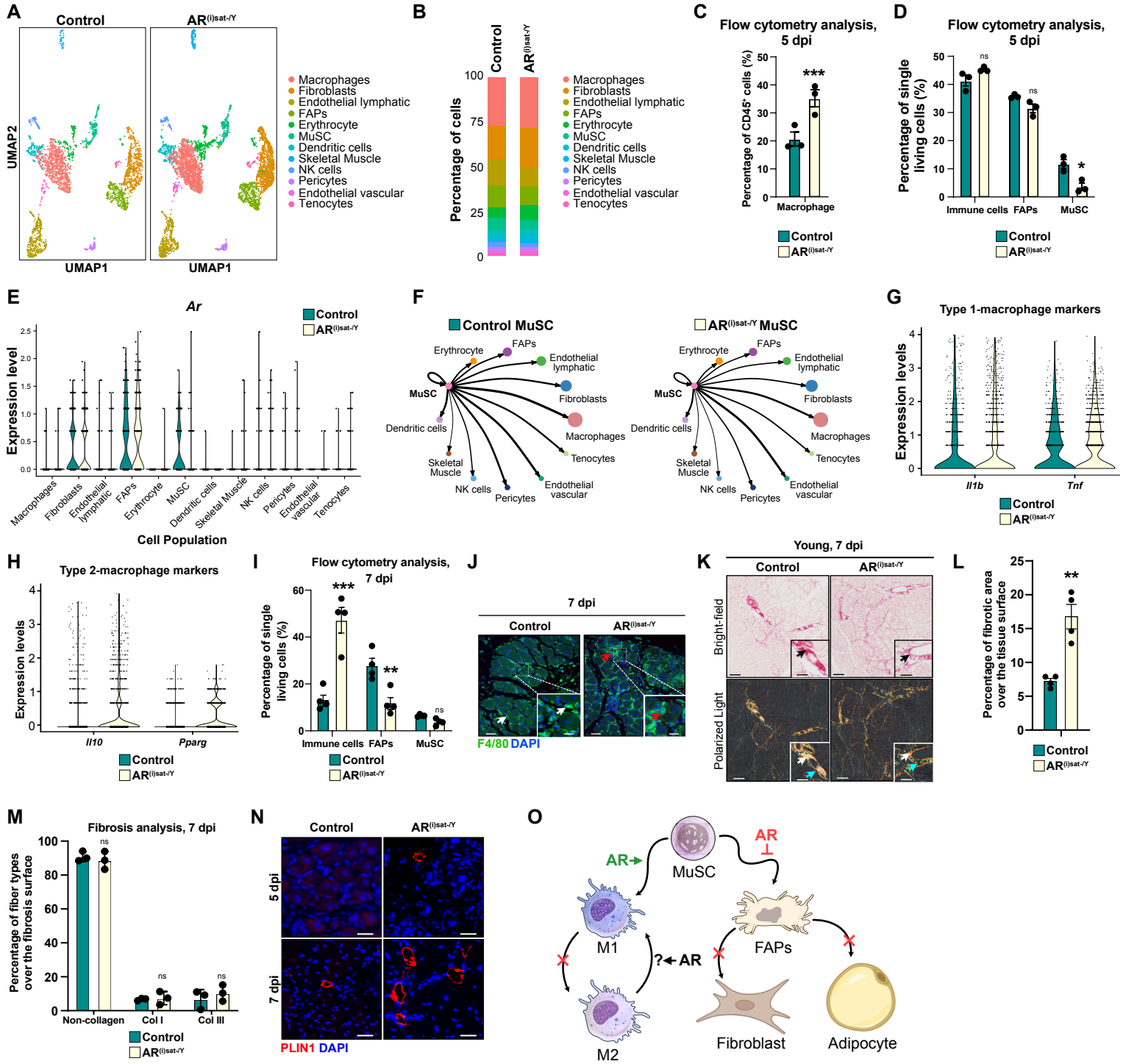
A
Control
AR(i)sat-/Y
UMAP2
UMAP1
UMAP1
Macrophages
Fibroblasts
Endothelial lymphatic
FAPs
Erythrocyte
MuSC
Dendritic cells
Skeletal Muscle
NK cells
Pericytes
Endothelial vascular
Tenocytes
B
Control
AR(i)sat-/Y
Percentage of cells
100
75
50
25
0
C
Flow cytometry analysis, 5 dpi
Percentage of CD45+ cells (%)
***
Macrophage
Control
AR(i)sat-/Y
D
Flow cytometry analysis, 5 dpi
Percentage of single living cells (%)
ns
ns
*
Immune cells
FAPs
MuSC
Control
AR(i)sat-/Y
E
Ar
Control
AR(i)sat-/Y
Expression level
Cell Population
F
Control MuSC
AR(i)sat-/Y MuSC
Erythrocyte
FAPs
Endothelial lymphatic
MuSC
Fibroblasts
Dendritic cells
Macrophages
Tenocytes
Skeletal Muscle
NK cells
Pericytes
Endothelial vascular
G
Type 1-macrophage markers
Expression levels
Il1b
Tnf
Control
AR(i)sat-/Y
H
Type 2-macrophage markers
Expression levels
Il10
Pparg
Control
AR(i)sat-/Y
I
Flow cytometry analysis, 7 dpi
Percentage of single living cells (%)
***
**
ns
Immune cells
FAPs
MuSC
Control
AR(i)sat-/Y
J
7 dpi
Control
AR(i)sat-/Y
F4/80 DAPI
K
Young, 7 dpi
Control
AR(i)sat-/Y
Bright-field
Polarized Light
L
Percentage of fibrotic area over the tissue surface
**
Control
AR(i)sat-/Y
M
Fibrosis analysis, 7 dpi
Percentage of fiber types over the fibrosis surface
ns
ns
ns
Non-collagen
Col I
Col III
Control
AR(i)sat-/Y
N
Control
AR(i)sat-/Y
5 dpi
7 dpi
PLIN1 DAPI
O
MuSC
AR
AR
M1
?
AR
FAPs
M2
Fibroblast
Adipocyte

FIGURE 4

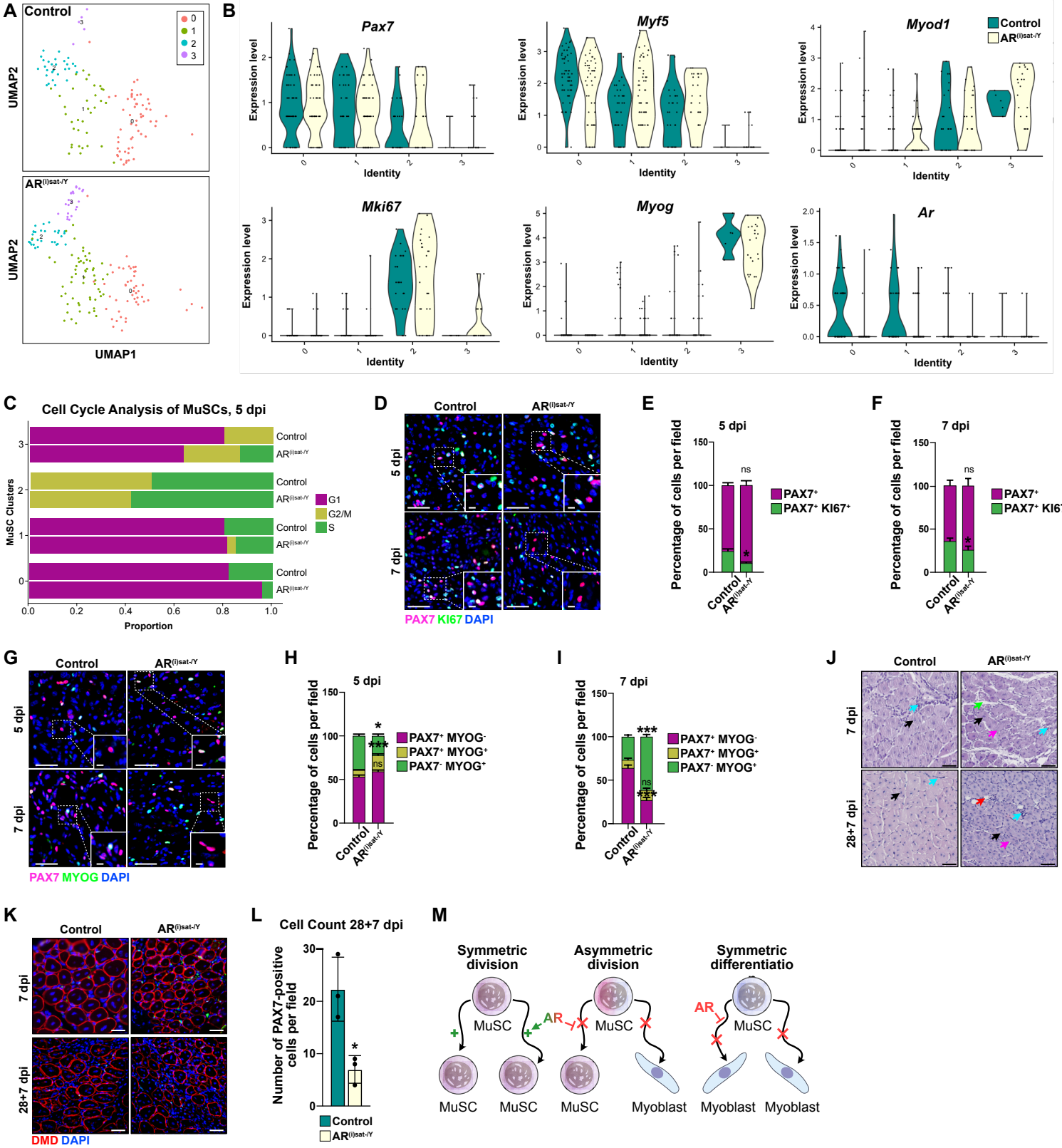
A
Control
AR(i)sat-/Y
UMAP2
UMAP1
B
Pax7
Myf5
Myod1
Mki67
Myog
Ar
Expression level
Identity
Control
AR(i)sat-/Y
C
Cell Cycle Analysis of MuSCs, 5 dpi
MuSC Clusters
Proportion
G1
G2/M
S
D
Control
AR(i)sat-/Y
5 dpi
7 dpi
PAX7 KI67 DAPI
E
5 dpi
Percentage of cells per field
PAX7+
PAX7+ KI67+
ns
F
7 dpi
G
Control
AR(i)sat-/Y
5 dpi
7 dpi
PAX7 MYOG DAPI
H
5 dpi
PAX7+ MYOG-
PAX7+ MYOG+
PAX7- MYOG+
I
7 dpi
J
7 dpi
28+7 dpi
K
7 dpi
28+7 dpi
DMD DAPI
L
Cell Count 28+7 dpi
Number of PAX7-positive cells per field
M
Symmetric division
Asymmetric division
Symmetric differentiatio
MuSC
AR
Myoblast

FIGURE 5

A

AR Known Motif Search

Name	Logo	p-value	% of Targets
ARE		1e-55	26.2 %
AR-half site		1e-68	39.5%

AR *de novo* Motif Search

Name	Logo	p-value	% of Targets
AR		1e-348	47.15 %

B

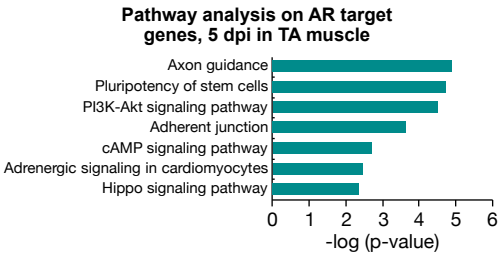

C

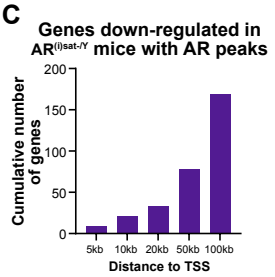

D

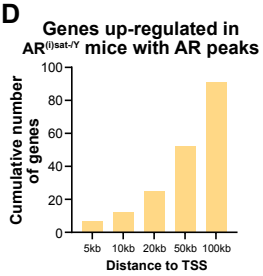

E

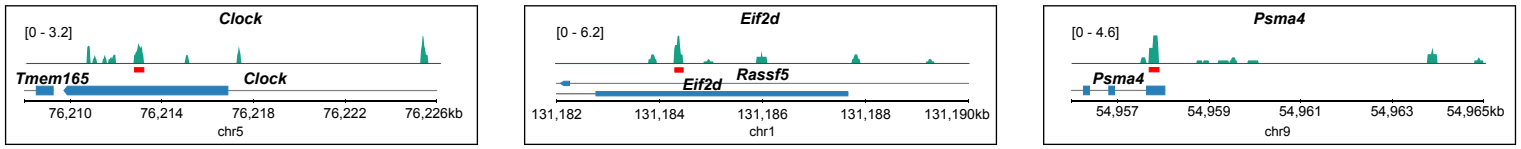

F

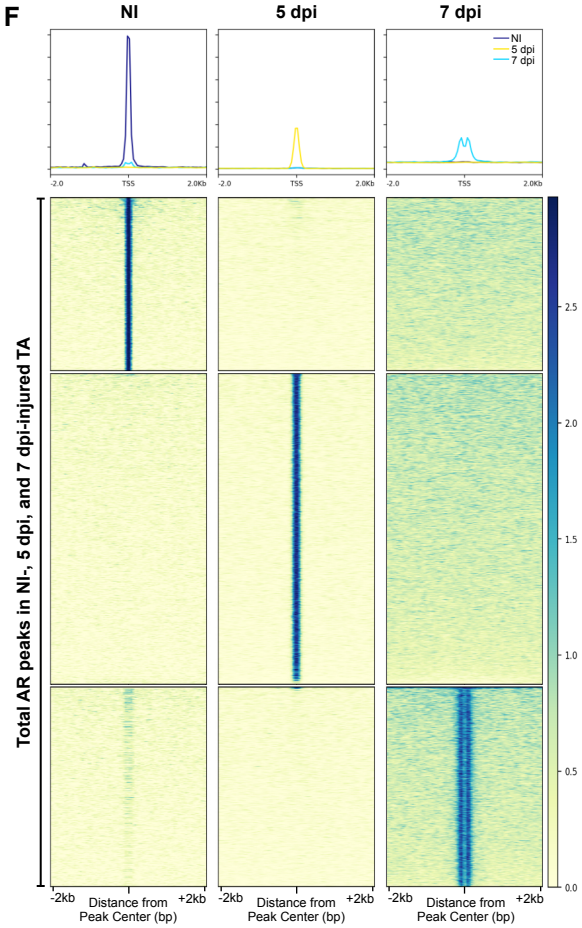

G

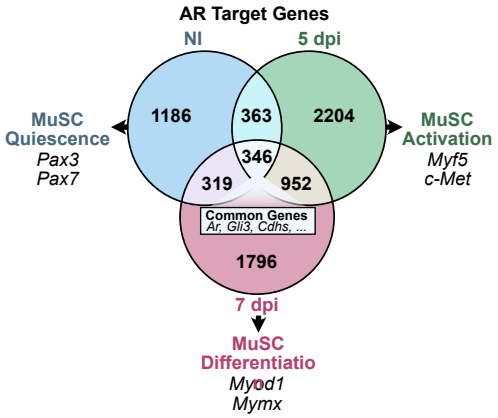

H

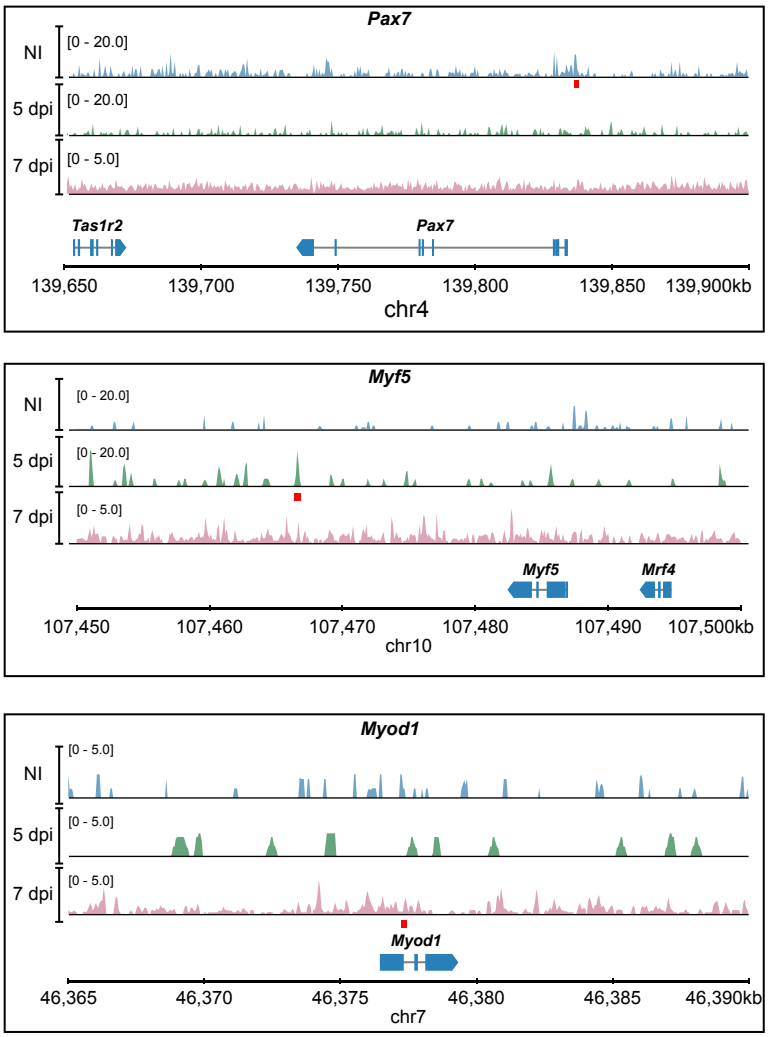

I

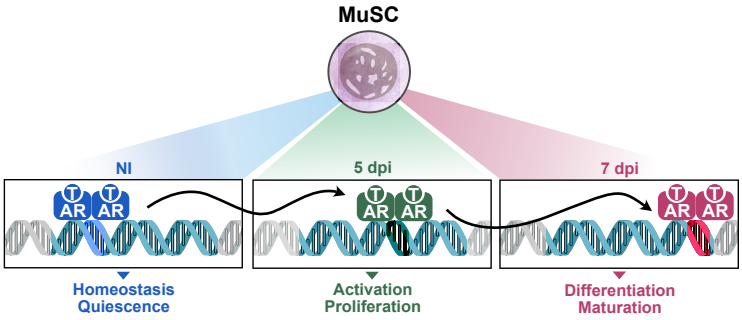

FIGURE 6

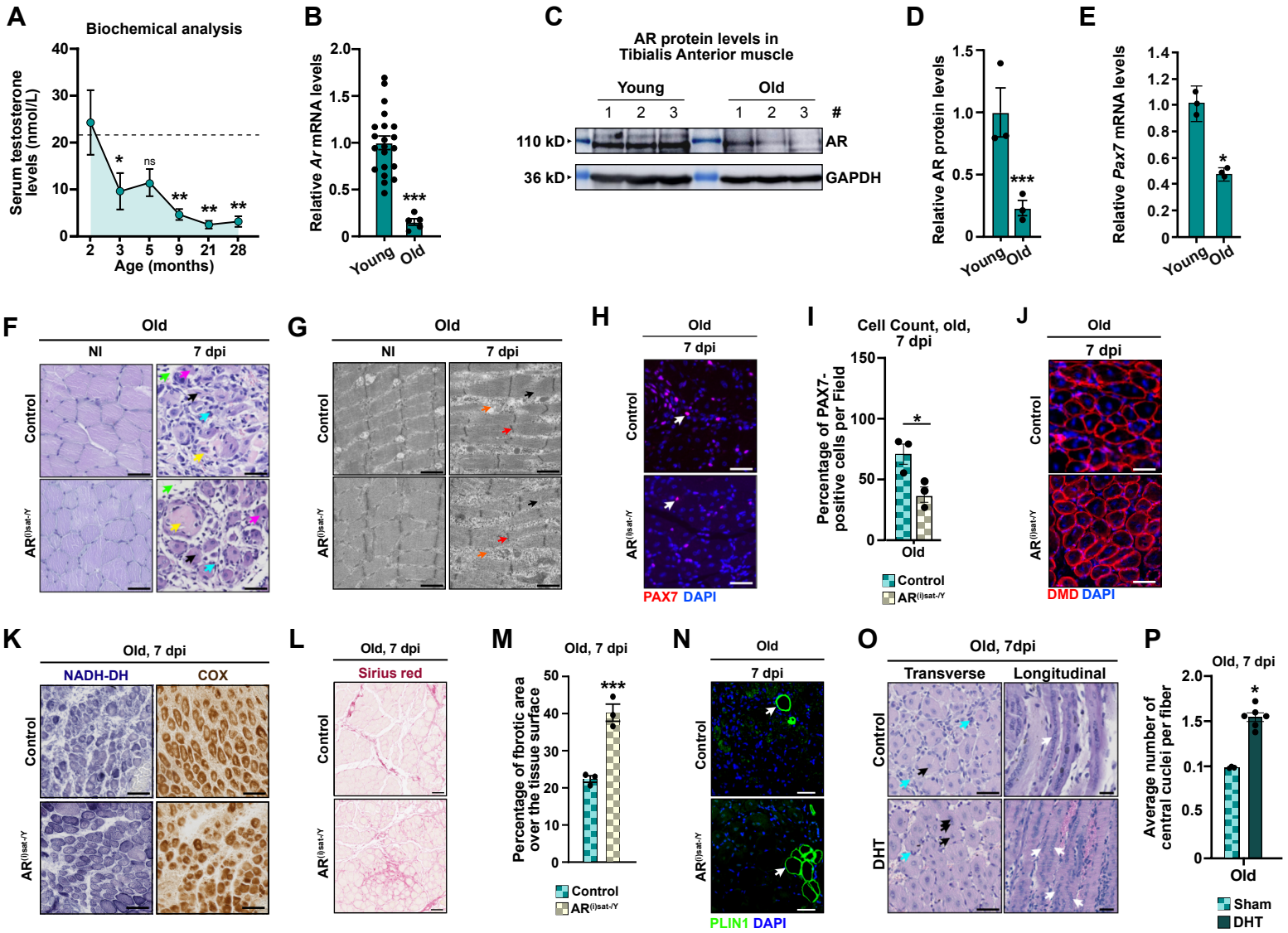
A
Biochemical analysis
Serum testosterone levels (nmol/L)
Age (months)
B
Relative Ar mRNA levels
Young
Old
C
AR protein levels in Tibialis Anterior muscle
Young
Old
110 kD
36 kD
AR
GAPDH
D
Relative AR protein levels
E
Relative Pax7 mRNA levels
F
Old
NI
7 dpi
Control
AR(i)sat-/Y
G
H
PAX7 DAPI
I
Cell Count, old, 7 dpi
Percentage of PAX7-positive cells per Field
J
DMD DAPI
K
Old, 7 dpi
NADH-DH
COX
L
Sirius red
M
Percentage of fibrotic area over the tissue surface
N
PLIN1 DAPI
O
Transverse
Longitudinal
DHT
P
Average number of central cuclei per fiber
Sham
DHT

FIGURE 7

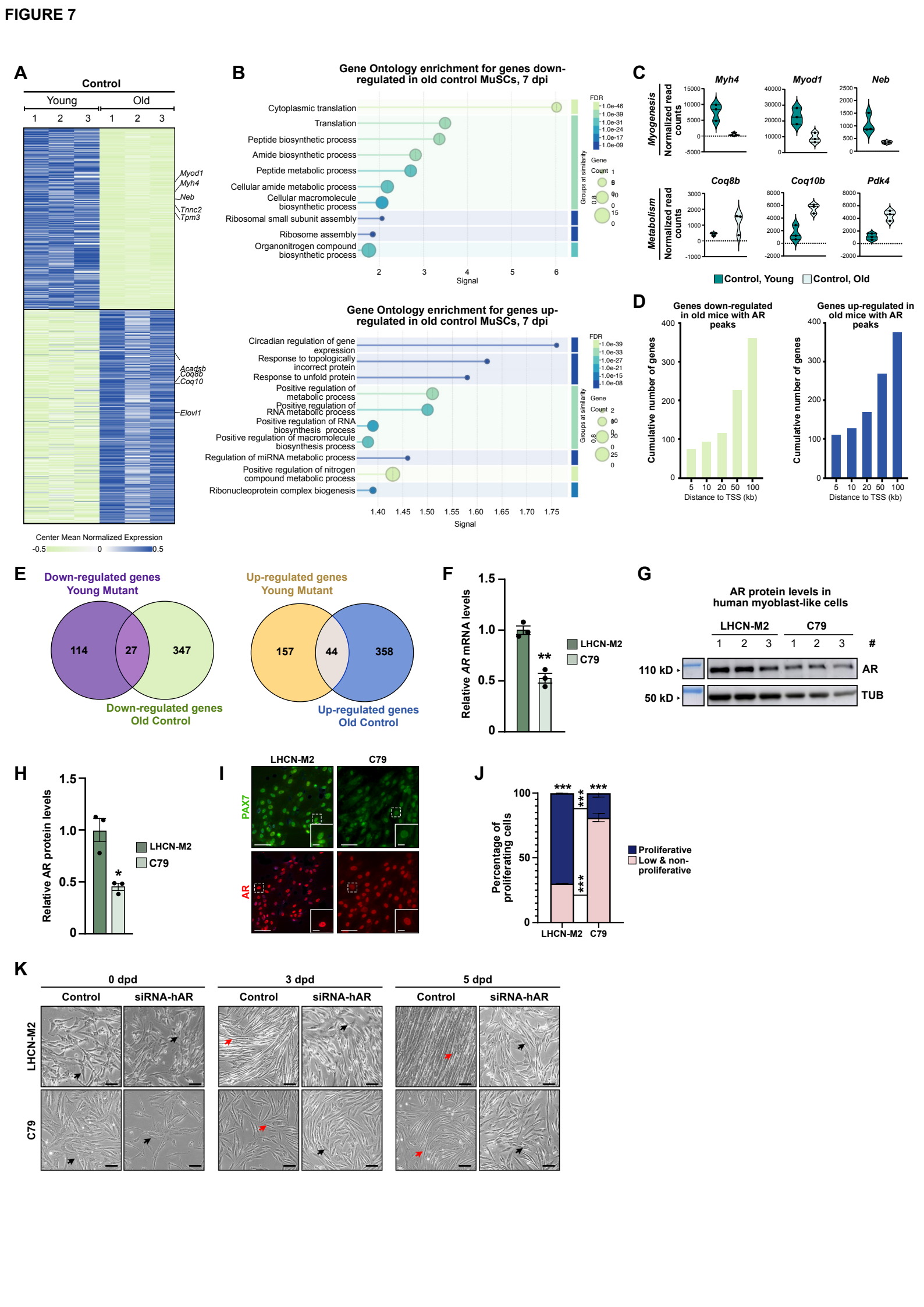
A
Control
Young
Old
1 2 3 1 2 3
Myod1
Myh4
Neb
Tnnc2
Tpm3
Acadsb
Coq8b
Coq10
Elovl1
Center Mean Normalized Expression
-0.5 0 0.5
B
Gene Ontology enrichment for genes down-regulated in old control MuSCs, 7 dpi
Cytoplasmic translation
Translation
Peptide biosynthetic process
Amide biosynthetic process
Peptide metabolic process
Cellular amide metabolic process
Cellular macromolecule biosynthetic process
Ribosomal small subunit assembly
Ribosome assembly
Organonitrogen compound biosynthetic process
Signal
FDR
Gene Count
Groups at similarity
Gene Ontology enrichment for genes up-regulated in old control MuSCs, 7 dpi
Circadian regulation of gene expression
Response to topologically incorrect protein
Response to unfold protein
Positive regulation of metabolic process
Positive regulation of RNA metabolic process
Positive regulation of RNA biosynthesis process
Positive regulation of macromolecule biosynthesis process
Regulation of miRNA metabolic process
Positive regulation of nitrogen compound metabolic process
Ribonucleoprotein complex biogenesis
C
Myogenesis
Metabolism
Normalized read counts
Myh4
Myod1
Neb
Coq8b
Coq10b
Pdk4
Control, Young
Control, Old
D
Genes down-regulated in old mice with AR peaks
Genes up-regulated in old mice with AR peaks
Cumulative number of genes
Distance to TSS (kb)
E
Down-regulated genes Young Mutant
114
27
347
Down-regulated genes Old Control
Up-regulated genes Young Mutant
157
44
358
Up-regulated genes Old Control
F
Relative AR mRNA levels
LHCN-M2
C79
G
AR protein levels in human myoblast-like cells
LHCN-M2
C79
110 kD
50 kD
AR
TUB
H
Relative AR protein levels
LHCN-M2
C79
I
LHCN-M2
C79
PAX7
AR
J
Percentage of proliferating cells
Proliferative
Low & non-proliferative
LHCN-M2
C79
K
0 dpd
3 dpd
5 dpd
Control
siRNA-hAR
LHCN-M2
C79